https://doi.org/10.5194/bg-2019-315
Preprint. Discussion started: 4 September 2019
© Author(s) 2019. CC BY 4.0 License.

Biogeosciences Discussions
Open Access
EGU

Formation and origin of Fe-Si oxyhydroxide deposits at the ultra-slow spreading Southwest Indian Ridge

Authors:

Kaiwen Ta[1, 2], Zijun Wu[1*], Xiaotong Peng[2] and Zhaofu Luan[1]

[1]School of Ocean and Earth Science and State Key Laboratory of Marine Geology, Tongji University, Shanghai, China,

[2]Deep Sea Science Division, Institute of Deep Sea Science and Engineering, Chinese Academy of Sciences, Sanya, China.

Corresponding author:

Zijun Wu, (wuzj@tongji.edu.cn)

Abstract

Low-temperature hydrothermal system is dominated by Fe-Si oxyhydroxide deposits. However, the formation process and mechanism on modern hydrothermal Fe-Si oxyhydroxides at ultra-slow spreading centers remain poorly understood. The investigation presented in this paper focuses on six Fe-Si deposits collected from different sites at the Southwest Indian Ridge (SWIR). The mineralogical and geochemical evidence showed significant characteristics of a low-temperature hydrothermal origin. The Mössbauer spectra and iron speciation data further provided

https://doi.org/10.5194/bg-2019-315
Preprint. Discussion started: 4 September 2019
© Author(s) 2019. CC BY 4.0 License.

Biogeosciences
Discussions
Open Access
EGU

an insight into iron-bearing phases in all deposits. Two different types of biomineralized forms were discovered in these deposits by Scanning Electron Microscopy analysis. Energy-dispersive X-ray spectrometry and nano secondary ion mass spectrometry revealed that distinct biogenic structures were mainly composed of Fe, Si, and O, together with some trace elements. The Sr and Nd isotope compositions of Fe-Si deposits at the SWIR were closely related to interaction between hydrothermal fluids and seawater. The remarkably homogeneous Pb isotope compositions can be attributed to hydrothermal circulation. Based on these findings, we suggest that microbial activity plays a significant role in the formation of Fe-Si oxyhydroxides at the at ultra-slow spreading SWIR. Biogenic Fe-Si oxyhydroxides potentially provide insights into the origin and evolution of life in the geologic record.

1 Introduction

Hydrothermal Fe-Si-oxyhydroxide deposits are widespread in many geological settings, such as mid-ocean ridges (Alt, 1988; Benjamin et al., 2006; Dekov et al., 2010; Peng et al., 2015), back-arc spreading centers (Iizasa et al,. 1998; Hein et al., 2008; Sun et al., 2012), seamounts (Karl et al., 1989; Boyd and Scott, 2001; Emerson and Moyer, 2002; Singer et al., 2011), and intra-plate submarine volcanoes (Edwards et al., 2011; Fleming et al., 2013). Fe-Si oxyhydroxides in the form of yellowish to brown chimneys, mounds and flat-lying deposits have often been observed in low-temperature hydrothermal fields (Emerson and Moyer, 2002; Peng et al., 2015; Johannessen et al., 2016; Ta et al., 2017). In general, modern low-temperature

https://doi.org/10.5194/bg-2019-315
Preprint. Discussion started: 4 September 2019
© Author(s) 2019. CC BY 4.0 License.


hydrothermal systems are the product of diffuse hydrothermal fluids and/or the conductive cooling of high-temperature hydrothermal fluids mixed with seawater (German et al., 1990). A pronounced excess of ferrous iron and dissolved silica are typical characteristics of hydrothermal vent fluids (Tivey, 2007). Low-temperature hydrothermal Fe-Si oxyhydroxides are considered as important hydrothermal products which reflect the diffusion and evolution of hydrothermal fluids. The mineralogical and geochemical compositions of such deposits have provided insight into their formation mechanisms (Dekov et al., 2010; Sun et al., 2015; Ta et al., 2017). Recently, studies focused on the origin of Fe-Si-oxyhydroxides have been increasing, however little is currently known about the links between these deposits and microbial activity at the ultra-slow spreading Southwest Indian Ridge (SWIR).

The ultra-slow spreading SWIR represents the longest segment of the world's slowest-spreading ridge (German et al., 2010; Husson et al., 2015). The SWIR is characterized by a spreading rate of approximately 12–15 mm/yr, a lack of transform faults, and extensive exposures of mantle peridotites (Dick et al., 2003; Niu et al., 2015). Compared to fast-spreading ridge systems, hydrothermal activity along the ultra-slow spreading SWIR may have greater chemical and thermal fluxes (German et al., 2010). However, the composition and depth of oceanic crust at the SWIR seems to be different in many respects from average oceanic crust, and the data suggest the presence of thickened crust or a large thermal anomaly in the region (Sauter et al., 2009; Zhang et al., 2013; Niu et al. 2015). The diversity in styles of hydrothermal vents at the SWIR has been of particular interest, particularly the activity of

https://doi.org/10.5194/bg-2019-315
Preprint. Discussion started: 4 September 2019
© Author(s) 2019. CC BY 4.0 License.

high-temperature and low-temperature vents (German et al., 1998; Tao et al., 2012). Isotope analyses of mid-ocean ridge basalts have revealed a clear distinction between the Southwest Indian ridge and the Pacific and Atlantic ridge compositions (Hamelin and Allègre, 1985; Vlastélic et al., 1999). Previous studies have confirmed that plume-ridge interactions have produced geochemical and geophysical anomalies along the Indomed and Gallieni fracture zones beneath the SWIR (Breton et al., 2013; Yang et al., 2017). Recently, increasing attention has been paid to the petrology, element geochemistry, microbial communities and biogeography of the SWIR (Li et al., 2015; Chen et al., 2016; Ji et al., 2017; Zhou et al., 2018; Zhang et al., 2018). Although microbial activity was revealed to play an important role in the formation of Fe and Si minerals in low-temperature hydrothermal fields (Dekov et al., 2010), there are a few studies that show the presence of biomineralized structures encrusted by Fe-Si oxyhydroxides in the SWIR hydrothermal systems, indicating the oxyhydroxide deposits may also be of biogenic origin (Peng et al., 2011; Sun et al., 2015).

Here, we report the geochemical and geomicrobiological characterization of Fe-Si deposits from the ultra-slow spreading SWIR. Scanning electron microscope (SEM), X-ray diffraction (XRD), inductively coupled plasma-mass spectrometry (ICP-MS), nano secondary ion mass spectrometry (nanoSIMS), Pb-Sr-Nd-O isotopic analysis, Mössbauer Spectroscopy, and sequential iron mineral extraction experiments were used to investigate: (1) the geochemical and morphological characteristics of biogenic Fe-Si oxyhydroxides, (2) the role of microbial activity in the formation of

https://doi.org/10.5194/bg-2019-315
Preprint. Discussion started: 4 September 2019
© Author(s) 2019. CC BY 4.0 License.

the Fe-Si oxyhydroxides, (3) the implications of the Sr-Nd-Pb isotopic content of the low-temperature Fe-Si deposits at the ultra-slow spreading SWIR.

2 Geological Setting

This study is focused on the ultra-slow spreading Southwest Indian ridge segments 27 and 28, as defined by Cannat et al. (1999), incorporating the Indomed and Gallieni Fracture Zones (46.0 °E to 52.0 °E), where the central shallow section of the SWIR has an overall 15° obliquity. Geophysical and geochemical data have shown that this area is a V-shaped shallow domain associated with thickened crust and robust magmatism (Lin and Zhang., 2006). Tectonic and volcanic processes result in the growth of the oceanic crust at the SWIR (Niu et al. 2015; Li et al., 2015). Previous geological surveys have indicated that the robust melt supply may be associated with the Marion and Crozet hotspots (Georgen et al., 2001; Sauter et al., 2009). A study by Yu et al. (2018) showed that segments 27 and 28 of the ridge had contrasting tectonic and magmatic processes. An inactive hydrothermal field was discovered near the center of segment 27 (Zhao et al., 2013). The axial depth of this segment has become shallower and experienced a dramatic increase in magma supply since 8–11 Ma (Sauter et al., 2009). However, the Longqi hydrothermal field of segment 28, at 49.6 °E, has been confirmed to remain active, at a water depth of around 2750 m (Tao et al., 2012).

3 Materials and Methods

3.1 Sample Collection and Sample Descriptions

https://doi.org/10.5194/bg-2019-315
Preprint. Discussion started: 4 September 2019
© Author(s) 2019. CC BY 4.0 License.

Biogeosciences Discussions

Fragile and porous hydrothermal deposits (samples 20V-T8, 21V-T1, 21V-T7 and 33II-T2) were collected by a TV grabber during a cruise of the R/V DaYang YiHao conducted by the China Ocean Mineral Resource R&D Association (COMRA) at the SWIR, from 2008 to 2015. The yellowish 21V-T1 and brown 21V-T7 samples were located ~20 km north of the SWIR, and the brown 20V-T8 sample was located ~8 km to the north. The purple-red 34II-T22 sample was collected from the axis of the SWIR. Sample DIV95 was recovered from the Longqi field by the Human Occupied Vehicle (HOV) 'Jiaolong' diving cruise in 2015. This sample was very friable with a layered structure. The layers were nearly parallel and displayed an obvious color change (Fig. 2a). The upper layer of DIV95 was thin (~2–3 cm), and composed of orange-yellowish Fe-Si oxyhydroxides, whereas the bottom portion comprised a thicker (~3–5 cm), black layer of mixed Fe-Si oxyhydroxides and Mn-oxides. After recovery, the fresh samples were immediately divided into subsamples for mineralogical, geochemical and microscopic analyses. A small amount of the subsamples to be used for SEM analysis were fixed with 8% formaldehyde at −20 °C in sterile bags, and a separate amount was stored at 4 °C prior to nanoSIMS analysis. The rest of the samples were stored in anoxic hermetic bags at −20 °C to avoid oxidation.

3.2 Analytical Methods

3.2.1 Bulk Chemistry

Chemical compositions of the samples were determined by X-ray fluorescence (XRF) spectrometry and ICP-MS. Major elements were measured using XRF

https://doi.org/10.5194/bg-2019-315
Preprint. Discussion started: 4 September 2019
© Author(s) 2019. CC BY 4.0 License.


spectrometry (Shimadzu XRF-1800) with operating conditions of 40 kV and 95 mA. Six samples were powdered to 200 mesh size for major elements analysis. Powdered samples were then leached twice in 6 M HCI for 2 hours at 100 °C, followed by ultrasonic leaching in Milli-Q water. Major elements were analyzed quantitatively after the fusion of 0.1 g of sample material with 3.6 g of dilithium tetraborate at 1050 °C for 16 min. Trace and rare earth element compositions of the samples were determined by ICP-MS using a Thermo VG-X7 mass spectrometer. Samples were dissolved using a solution of HNO_3 + HF on a hot plate. The eluted samples were diluted by 2% HNO_3 for trace element quantification (Peng et al., 2011). The precision determined from sample duplicates, as well as from repeated analyses, was better than 5%.

3.2.2 Mineralogy

XRD was employed to characterize the mineralogy of the particles of interest. Samples were freeze dried under anoxic conditions to avoid oxidation during drying. The subsamples were thoroughly ground using a pestle and a mortar, followed by analyses using a D/max2550VB3+/PC X-ray diffractometer (Rigaku Corporation) with Cu Kα radiation at 35 kV and 30 mA. Diffraction angles corresponding to the unique crystal structure of each mineral were measured. The scan speed was 2° 2θ/min, and the resolution was 0.02° 2θ.

3.2.3 Morphological Diversity

SEM was employed to determine the morphological diversity of the hydrothermal deposits. Freeze-dried subsamples were fixed onto aluminum stubs with

https://doi.org/10.5194/bg-2019-315
Preprint. Discussion started: 4 September 2019
© Author(s) 2019. CC BY 4.0 License.

two-way adherent tabs and allowed to dry overnight. Subsequently, the samples were sputter coated with gold for 30 seconds. All samples were examined using an FEI Apreo SEM equipped with an EDAX energy-dispersive X-ray spectrometer (EDS). The SEM was operated at 2 kV with a working distance of 10 mm to facilitate optimum image collection whilst minimizing charging and sample damage. For EDS analyses, an accelerating voltage of 20 kV was used to generate sufficient X-ray counts.

3.2.4 Pb-Sr-Nd isotopes

Sr, Nd, and Pb isotopic compositions were quantified in the Laboratory for Radiogenic Isotope Geochemistry at the University of Science and Technology of China, using a Phoenix-Thermal Ionization Mass Spectrometer (Isotopx, UK) for Sr and Nd analysis, and an IsoProbe-Thermal Ionization Mass Spectrometer (GV [formerly Micromass], UK) for analysis of Pb. The detailed analytical procedure for Nd, Pb, and Sr isotopic measurements follows that described by Chen et al. (2000, 2007). Sample powders (~100 mg) used for isotopic analysis were dissolved in HNO_3 + HF solution, and then transferred to a 6 M HCl solution. Pb was fixed to Ta filaments using Si-gel. Sr was loaded onto preconditioned Ta filaments using a Ta-HF activator. Nd was loaded as phosphate onto preconditioned Re filaments. Sr and Nd isotopic ratios were normalized to an $^{86}Sr/^{88}Sr$ of 0.1194 and an $^{143}Nd/^{144}Nd$ of 0.7219 during runtime. Measured values for the NBS 987 Sr and La Jolla Nd standards were 0.710265 ± 12 (2σ) for $^{86}Sr/^{88}Sr$, and 0.511862 ± 10 (2σ) for $^{143}Nd/^{144}Nd$. The Pb isotope data were periodically checked against NBS 981, which produced means of

https://doi.org/10.5194/bg-2019-315
Preprint. Discussion started: 4 September 2019
© Author(s) 2019. CC BY 4.0 License.


$^{206}Pb/^{204}Pb = 16.9416 \pm 13$ (2σ), $^{207}Pb/^{204}Pb = 15.500 \pm 13$ (2σ) and $^{208}Pb/^{204}Pb = 36.7262 \pm 31$ (2σ) (Baker et al., 2004). The internal precision of Pb isotope data was estimated to be less than 0.03%.

3.2.5 Oxygen Isotope Analysis

Six freeze-dried samples powdered to 200 mesh size were purified using the following procedure. Carbonate was treated using 10% (vol/vol) acetic acid by sonication for 2 h. The Fe and Mn oxides were removed using a mixture of 1 M hydroxylamine hydrochloride and 25% (vol/vol) acetic acid. Organic matter was digested by adding aqua regia. The final detritus was rinsed three times with distilled water and dried in an oven at approximately 55 °C. Stable oxygen isotope analyses were performed using a MAT-253 mass spectrometer at the Institute of Mineral Resources, Chinese Academy of Geological Sciences, China. Oxygen isotope data were collected from approximately 20 mg purified samples, using CO_2 generated from silicates by heating the powder with a CO_2 laser, using BrF_5 as the fluorinating reagent (Cole et al., 2004). The resultant oxygen was converted to CO_2 on a platinum-coated carbon rod. The isotopic data are reported relative to the Standard Mean Ocean Water (SMOW) with a precision of 0.2‰.

3.2.6 Fe behavior and oxidation state

The ^{57}Fe Mössbauer spectra of six homogenized samples were recorded in transmission geometry using a conventional constant-acceleration spectrometer. An 8 mCi activity ^{57}Co source supplied γ rays for the measurements. The spectra were recorded at room temperature. The spectrometer was calibrated using a standard α-Fe

https://doi.org/10.5194/bg-2019-315
Preprint. Discussion started: 4 September 2019
© Author(s) 2019. CC BY 4.0 License.

Biogeosciences Discussions Open Access EGU

foil, and the reported isomer shifts are relative to the center of the α-Fe spectrum. The fit of the Mössbauer spectra was evaluated using doublets of Loretzian peaks via the least squares method, with the WinNormos-for-Igor 3.0 program. The ideal adsorber thickness values were generated with the *Recoil* program (Lagarec and Rancourt, 1998).

3.2.7 Iron Speciation

Iron speciation was extracted from the deposits following the sequential extraction technique developed by Poulton and Canfield (2005). In brief, approximately 0.5 g of each dried SWIR sample was accurately weighed. The samples were powdered and added to Teflon tubes. The samples were then mixed with the appropriate solvent for a defined period of time (Table 4). Subsequently, the samples were centrifuged at 4000 rpm. The extraction was decanted and filtered through a 0.2 μm membrane. Between each step, the samples were washed with distilled water. Iron concentrations in the extracts were determined using an Inductively Coupled Plasma Atomic Emission Spectrometer (ICP-AES, Perkin Elmer Optima 3000) with a relative standard deviation of less than 2%. The contents of all samples were normalized to extracted dry deposits (μg/g).

3.2.8 Ion Distribution

NanoSIMS was employed to characterize the nanometer- to micrometer-scale distribution of $^{12}C^-$, $^{12}C^{14}N^-$, $^{32}S^-$, $^{27}Al^{16}O^-$, $^{55}Mn^{16}O^-$ and $^{56}Fe^{16}O_2^-$ in Fe-Si deposits that were spread on glass slides. NanoSIMS analyses were performed at the Institute of Geology and Geophysics, Chinese Academy of Sciences, using a CAMECA

https://doi.org/10.5194/bg-2019-315
Preprint. Discussion started: 4 September 2019
© Author(s) 2019. CC BY 4.0 License.

NanoSIMS 50 L (CAMECA, Paris, France). This nanoSIMS is capable of sub-50 nm lateral resolution while imaging negatively charged secondary ions, are samples have been sputtered with Cs^+ primary ions. Each region of interest was presputtered using a 150 pA beam current and an ion dose of $N > 5 \times 10^{16}$ ions/cm^2 (Gnaser, 2003). This treatment removed any surface contaminants, implanted Cs^+ ions into the sample matrix, and enabled an approximately steady state of ion emission to be reached. Using a Cs^+ primary beam, negative secondary ions ($^{12}C^-$, $^{12}C^{14}N^-$, $^{32}S^-$, $^{27}Al^{16}O^-$, $^{55}Mn^{16}O^-$ and $^{56}Fe^{16}O_2^-$) were sputtered from the sample surface with a beam current of c.2.5 pA, and were detected in multicollection mode (Ta et al., 2017).

4 Results

4.1 Geochemistry

Major and trace element compositions of the Fe-Si deposits are presented in Table 1. All analyzed deposits had Fe_2O_3 contents ranging from 11.56 to 64.33 wt%, and SiO_2 contents ranging from 27.22 to 80.20 wt%. The highest Fe_2O_3 and SiO_2 concentrations were found in the purple-red 34II-T22 and brown 20V-T8 deposits, respectively. The two subsamples of DIV95 showed different chemical compositions. The MnO_2 concentration of the black layer of DIV95-2 was 30.13 wt%, while the content of SiO_2 in DIV95-2 was lower than in DIV95-1. The deposits displayed limited variability in their P_2O_5 content, which ranged from 0.149 to 0.898 wt%. The Fe/Mn ratios of the deposits varied over a broad range from 1.41 to 723.53, and the Al/(Al + Fe + Mn) ratios were extremely low (< 0.003).

https://doi.org/10.5194/bg-2019-315
Preprint. Discussion started: 4 September 2019
© Author(s) 2019. CC BY 4.0 License.

Biogeosciences Discussions Open Access EGU

The studied deposits contained very low amounts of the majority of trace elements and REEs. The values of total rare earth elements (ΣREE) in the different deposits varied from 1.135 to 18.96 ppm, with an average of 7.67 ppm. The concentration of ΣREE in the 34II-T22 sample was the highest of all deposits. The REE distribution patterns of the Fe-Si deposits exhibited both negative Ce and positive Eu anomalies. The deposits showed a slight enrichment in light REE (LREE) relative to heavy REE (HREE) (Fig. 2). Fe-Si deposits had significantly higher large-ion lithophile element (such as Sr, U, Rb and Ba) contents than high field strength element (such as Hf, Th, Ta and Nb) contents. The 34II-T22 sample was noticeably enriched in trace elements such as Pb, V, Cu, Co, Ni, Zn, and U, but depleted in Li and Ba, relative to the other samples. The Fe_2O_3/SiO_2 ratios of the 21V-T1 and 21V-T7 deposits showed a narrow range (0.32–0.36), however the 20V-T8 deposits had the lowest Fe_2O_3/SiO_2 ratio of all deposits. The Fe/REE ratios of the deposits varied between 1.57 and 12.99. The 20V-T8 deposit, that was richer in Si and slightly depleted in Fe compared to the 34II-T22 deposit, also had lower compositions of the trace elements and REE relative to 34II-T22. Fe/Mn and Fe/REE ratios were lowest in the DIV95-1 and DIV95-2 samples.

The $\delta^{18}O$ values of all the deposits ranged between 16.56‰ and 35.87‰ (Table 2). The O isotopic composition of the hydrothermal deposits was reflected in the poorly crystalline Fe-Si oxyhydroxides, which precipitated from hydrothermal fluids. O isotopic fractionation is often used to calculate precipitation temperature in hydrothermal environments. We reference the $\delta^{18}O_{hydrothermal\ fluid}$ data of the Kairei

https://doi.org/10.5194/bg-2019-315
Preprint. Discussion started: 4 September 2019
© Author(s) 2019. CC BY 4.0 License.

hydrothermal field in the Central Indian Ridge (Gamo et al., 2001). The precipitation temperature was calculated by Kita et al. (1985). The calculated results indicate that the deposits would have precipitated at temperatures across the range 28.76–114.66 °C, which supports their low temperature origin.

The Sr-Nd-Pb isotopic compositions of the deposits are presented in Table 2 and Figure 7. The Sr isotopic compositions of the deposits showed only slight variation ($^{87}Sr/^{86}Sr$ = 0.707937–0.709150), and had values similar to present-day seawater ($^{87}Sr/^{86}Sr$ = 0.70917) (Burke et al., 1982). $^{143}Nd/^{144}Nd$ values of the deposits varied from 0.512332 to 0.512801, corresponding to εNd values ranging from -6 to 3.2. Positive εNd values implied the presence of an SWIR upper mantle component. Pb isotope compositions showed clear homogenization ($^{206}Pb/^{204}Pb$ = 18.2694–18.4829, $^{207}Pb/^{204}Pb$ = 15.5488–15.6404, $^{208}Pb/^{204}Pb$=38.2145–38.4493). In contrast, $^{207}Pb/^{204}Pb$ and $^{208}Pb/^{204}Pb$ ratios of the samples were found to be relatively high compared to SWIR and SEIR basalts (Figs. 7a–b). $^{206}Pb/^{204}Pb$ ratios of the deposits correlated well with $^{207}Pb/^{204}Pb$ and $^{208}Pb/^{204}Pb$, except for 21V-T7. The majority of SWIR deposit compositional data were clearly distinct from mid-Pacific and Antarctic Ridge basalts and Arctic marine sediments (Fig. 7). Additional details of the isotopic characteristics of the deposits were shown by plots of $^{87}Sr/^{86}Sr$ versus $^{143}Nd/^{144}Nd$ and $^{206}Pb/^{204}Pb$ (Fig.s 7c–d).The samples showed significant similarity to the low-temperature iron-silica-rich deposits from the mid-Atlantic ridge (Fig.s 7c–d). There was no overlap between the isotopic signature of our samples and other geological settings.

https://doi.org/10.5194/bg-2019-315
Preprint. Discussion started: 4 September 2019
© Author(s) 2019. CC BY 4.0 License.

285 **4.2 Mineralogy of Fe-Si deposits and Mössbauer Spectroscopy**

286 The XRD results showed that 2-line ferrihydrite, pyrite, natrojarosite, opal and
287 birnessite comprised the major minerals in the samples (Fig. S2). In the spectrum of
288 sample 33II-T8, a broad peak centered at 4.08 Å suggested the presence of opal. The
289 spectral peaks from samples 21V-T1, 21V-T7 and DIV 95-1 appeared at 3.83 Å and
290 2.21 Å, indicating the presence of pyrite. The spectral signature of birnessite was most
291 clearly observed in sample DIV95-2, at d = 7.06 and 2.45 Å. A small amount of
292 birnessite was observed in DIV95-1, which was presumed to be caused by the residual
293 black layer. Poorly crystalline two-line ferrihydrite, characterized by appearance
294 peaks at d = 2.62 Å and 1.51 Å, was the principal mineral observed in the spectra of
295 sample DIV95-2. Natrojarosite was also present in DIV95-1 and 21V-T7 deposits. In
296 addition, halite was observed in our samples, which presumably formed by
297 evaporation.

298 ^{57}Fe Mössbauer spectroscopy has been determined to be one of the most efficient
299 methods for studying the behavior and oxidation state of Fe (Murad and Schwertmann,
300 1980). The corresponding Mössbauer parameters and the identification of phases in
301 the spectra are presented in Figure 5 and Table 3. Fe^{3+} occurred primarily in four-fold
302 and six-fold coordination with oxygen, representing $^{IV}Fe^{3+}$ and $^{VI}Fe^{3+}$ components
303 (Burkhard, 2000). The Mössbauer spectrum of the DIV95-1 was fitted with two
304 quadrupole doublets. One doublet (IS = 0.59 mm/s, QS = 0.84 mm/s) was
305 characteristic of octahedrally-coordinated ferrihydrite (Murad and Johnston, 1987;
306 Murad and Cashion, 2004). The other doublet (IS = 0.33 mm/s, QS = 0.79 mm/s) was

https://doi.org/10.5194/bg-2019-315
Preprint. Discussion started: 4 September 2019
© Author(s) 2019. CC BY 4.0 License.


307 comparable to those of two-line ferrihydrite reported in previous studies (Murad and
308 Schwertmann, 1980; Johnston and Lewis, 1983; Murad and Johnston, 1987; Berquó et
309 al., 2007). Likewise, the Mössbauer spectrum of DIV95-2 was also fitted with two
310 different quadrupole doublets. One doublet (IS = 0.34 mm/s, QS = 0.55 mm/s) was
311 characteristic for lepidocrocite (Murad and Schwertmann, 1980; Murad, 1984). The
312 other doublet (IS = 0.34 mm/s, QS = 0.85 mm/s) was analogous to those of two-line
313 ferrihydrite reported in hydrothermal deposits (Peng et al., 2013). However, the
314 spectrum of the 34II-T22 was fitted with a single quadrupole doublet. Parameters of
315 IS (0.36 mm/s) and QS (0.72 mm/s) indicated that the doublet could be ascribed to
316 two-line ferrihydrite (Murad, 1988; Wade et al., 1999). Furthermore, parameters of IS
317 = 0.40 mm/s, QS = 0.65 mm/s and IS = 0.40 mm/s, QS = 1.11 mm/s for sample
318 21V-T1 were interpreted to reflect the presence of goethite and
319 octahedrally-coordinated ferrihydrite, respectively (Oh et al., 1998; Murad and
320 Schwertmann, 1980). The 21V-T7 sample showed two quadrupole doublets with IS =
321 0.34 mm/s, QS = 0.71 mm/s and IS = 0.56 mm/s, QS = 0.84 mm/s, corresponding to
322 two-line ferrihydrite and octahedrally-coordinated ferrihydrite, respectively (Oh et al.,
323 1998; Murad and Schwertmann, 1980). Moreover, sample 20V-T8 displays a further
324 type of Mössbauer spectrum, fitted using two quadrupole doublets. Values of IS =
325 0.40 mm/s, QS = 1.01 mm/s and IS = 0.40 mm/s, QS = 0.58 mm/s were in accordance
326 with those previously reported for lepidocrocite and ferrihydrite (Murad and
327 Schwertmann, 1980; Berquó et al., 2007).

328 **4.3 Sequential Iron Mineral Extraction**

https://doi.org/10.5194/bg-2019-315
Preprint. Discussion started: 4 September 2019
© Author(s) 2019. CC BY 4.0 License.


Sequential extraction of iron minerals identified four iron-bearing phases, as shown in Table 4 and Figure 6. Fe_{Carb}, the adsorbed iron and carbonate associated iron pool, was the least abundant of the iron-bearing phases, and varied between 11.38 μmol/g and 28.70 μmol/g. The proportion of Fe_{Carb} in the 34II-T22, 21V-T7 and 20V-T8 samples was higher than in DIV95-2 (Fig. 6). Fe_{OX1}, the easily reducible ferric iron oxide pool, mainly recorded the presence of ferrihydrite and lepidocrocite. Fe_{OX1} concentrations in the DIV95-1, 34II-T22, 21V-T7 and 20V-T8 samples were all similar, at approximately 111.71–118.48 μmol/g, with sample DIV95-2 having a much lower content of about 0.4 umol/g. Fe_{OX2}, the ferric iron (hydr)oxide pool, mainly recorded the presence of goethite and hematite. Fe_{OX2} concentrations of all deposits were very similar, varying from 218.13 to 226.51 μmol/g. The most abundant Fe-bearing phase was Fe_{PRS}, the poorly reactive sheet silicate pool in Fe-Si deposits. Sample DIV95-1 had a lower Fe_{PRS} concentration than sample DIV95-2, but was still rather high at about 647.46 μmol/g.

4.4 Microtextures, Micromorphologies and Compositions

SEM observations showed that different types of structures were abundant in the hydrothermal Fe-Si deposits. Morphologies included rod-like sheaths, rosette spherical structures, mineralized spheroids, ribbon-like helical filaments, threadlet filaments, branched structures and twisted stalks (Fig. 4). The orange-yellowish DIV95-1 deposit was primarily composed of mineralized rod-like forms with a network-like structure (Fig. 4a). However, the black DIV95-2 deposit was characterized by rosette spherical structures with a main component of Mn, according

https://doi.org/10.5194/bg-2019-315
Preprint. Discussion started: 4 September 2019
© Author(s) 2019. CC BY 4.0 License.

to EDS results (Fig. 4j). Spherical morphologies encrusted by iron and silicon were present in the yellowish 21V-T1 deposits (Fig. 4d). A wide morphological diversity of Fe-Si filamentous forms was also identified, including twisted filaments, curved filaments, and branched filaments. Filamentous structures were particularly abundant in the purple-red 34II-T22 and brown 21V-T7 deposits (Figs. 4e–g). The threadlet filaments had a diameter of 0.5 to 1 μm and were up to 100 μm in length (Fig. 4g). These filaments resemble the Fe oxyhydroxide stalks produced by the chemolithotrophic Fe-oxidizing bacterium *Marirpofundus ferrooxydans*. The hollow tube observed in sample 34II-T22 was about 10–50 μm in length and 1–3 μm in diameter (Fig. 4e), which is currently considered the characteristic trace of *Leptothrix ochracea*. In addition, branched sheaths and twisted stalks were also observed in 20V-T8 (Figs. 4h–i), with abundant spheroids scattered throughout the matrix of branched sheath structures (Fig. 4i). These mineralized sheaths and stalks are related to the metabolism of Fe-oxidizing bacteria previously reported in deep sea hydrothermal environments (Emerson and Moyer, 2010; Edwards et al., 2011; Peng et al., 2015; Johannessen et al., 2016; Chan et al., 2016). EDS analyses revealed that the branched sheaths and twisted stalks were composed of Fe, Si, and small amounts of Mg and Ca (Fig. 4l).

4.5 Isotopic Signals Revealed by nanoSIMS

The results of nanoSIMS mapping of Fe-stalk coming from sample 34II-T22 are shown in Figure 8. NanoSIMS has a higher sensitivity than SEM-EDS for most elements. In regions of interest, a pronounced intensity of $^{56}Fe^{16}O_2$ signals was

https://doi.org/10.5194/bg-2019-315
Preprint. Discussion started: 4 September 2019
© Author(s) 2019. CC BY 4.0 License.

observed in the stalk. The co-location of $^{56}Fe^{16}O_2$ and $^{27}Al^{16}O$ signals indicated that Fe and Al may originate from hydrothermal fluids and co-precipitated with the stalk. The elevated $^{55}Mn^{16}O$ signals were correlated with $^{56}Fe^{16}O_2$ signals, suggesting that Mn is probably formed through the adsorption of Mn onto the Fe-stalk. ^{12}C and $^{12}C^{14}N$ intensities are known to be very sensitive to biologically-derived materials (Herrmann et al., 2007). Therefore, the entire stalk was expected to show a high concentration of C and N elements, but ^{12}C and $^{12}C^{14}N$ signals were relatively low from this stalk. Although we observed more $^{12}C^{14}N$ signals than ^{12}C signals in the Fe-stalk, the yields of $^{12}C^{14}N$ secondary ions adjacent to the surrounding material were much higher.

5 Discussion

5.1 Origin of Fe-Si oxyhydroxide deposits at the SWIR

The Fe-Si oxyhydroxide deposits from the SWIR show mineralogy and chemical composition similar to those from other tectonic settings that have been interpreted to be of low temperature hydrothermal origin. The Fe-Si oxyhydroxides are characterized by enriched Fe and Si, along with low concentrations of Al and Ti (Table 1). Boström and Peterson (1969) indicated that hydrothermal deposits can display extremely low Al/(Al+ Fe+Mn) ratios (< 0.4), consistent with our results. Furthermore, the ternary diagrams of Fe-Mn-(Co + Ni + Cu) ×10 of our samples distinguished a hydrothermal, rather than hydrogenous or diagenetic, origin (Fig. 3a). Chondrite-normalized REE patterns of the Fe-Si oxyhydroxides showing positive Eu anomalies and slight LREE enrichment are typical characteristics of high-temperature hydrothermal fluids (Michard et al., 1983; Craddock et al., 2010). The lack of trace

https://doi.org/10.5194/bg-2019-315
Preprint. Discussion started: 4 September 2019
© Author(s) 2019. CC BY 4.0 License.


elements and REEs in the Fe-Si oxyhydroxides of this study indicates that they were rapidly precipitated from hydrothermal fluids with a small amount of content scavenged from ambient seawater (German et al., 1990). Mineral composition analysis also supports this view. In particular, the compositions of 2-line ferrihydrite, birnessite, pyrite and opal have been identified to be closely related to hydrothermal activity, as they are consistent with the compositions of other low temperature hydrothermal deposits (Boyd and Scott, 2001; Hein et al., 2008; Peng et al., 2011). The precipitation temperatures derived from ^{18}O isotope data further support the mixing and dilution of hydrothermal fluids and seawater.

Fe-Si oxyhydroxides are widespread in modern hydrothermal fields, such as the East Pacific Rise, Juan de Fuca Ridge, TAG hydrothermal field, Lilliput hydrothermal field, Wocan hydrothermal field, and Southern Mid-Atlantic ridge (Hekinian et al., 1993; Mills et al., 1996; Boyd and Scott, 2001; Hrischeva and Scott, 2007; Dekov et al., 2010; Sun et al., 2012). Hekinian et al. (1993) classified hydrothermal Fe-Si oxyhydroxides into four types based on their geological setting, morphology, mineralogy and composition (Fig. 3b). The ternary diagram of Fe-Si-(Co + Ni + Cu + Zn) x10 indicates that sample 33II-T22 falls within the Fe-rich field of type I (Si/Fe < 0.30, [Co + Ni + Cu + Zn] > 1000 ppm, Table 1). In contrast, the bulk composition of sample 20V-T8 is dominated by high Si and low Fe contents, and depleted in trace elements. Therefore, the 20V-T8 deposit enriched in amorphous opal belongs to type IV (Si/Fe = 5.4, [Co + Ni + Cu + Zn] < 1000 ppm, Table 1). Moreover, Fe-Si oxyhydroxide deposits from samples DIV95-1, DIV95-2, 21V-T7 and 21V-T1 all

https://doi.org/10.5194/bg-2019-315
Preprint. Discussion started: 4 September 2019
© Author(s) 2019. CC BY 4.0 License.

Biogeosciences Discussions

show intermediate enrichment in Fe and Si, so plot in the type III field (Si/Fe = 0.50–2.2, Table 1).

Previous studies have put forward different hypotheses for the formation of Fe-Si deposits in low-temperature hydrothermal environments, including i) the direct precipitation from hydrothermal fluids (Michard et al., 1984; Alt, 1988; Severmann et al., 2004), ii) alteration products of sulfides (Iizasa et al., 1998; Chaumba, 2017) or metalliferous sediments (Fortin et al., 1998; Hrischeva and Scott, 2007), and iii) biogenic Fe-Si oxyhydroxide (Toner et al., 2009; Devok et al., 2010; Peng et al., 2011; Bernis et al., 2012; Sun et al., 2012, 2015). Low Fe/Mn and Fe/REE ratios are a unique feature of samples DIV95-1 and DIV95-2 (Table 2). Some studies have demonstrated that Fe/Mn and REE/Fe ratios of deposits increased away from a hydrothermal source (Mitra et al., 1994; German et al., 2002; Edmonds and German, 2004). Therefore, the paragenetic sequences between Fe oxyhydroxides and Mn oxides of DIV95 may be attributed to the evolution of low-temperature diffuse fluids in the process of during discharge. This conclusion is supported by geological evidence from modern and ancient low-temperature hydrothermal fields (Severmann et al., 2004; Ta et al., 2017). We observed that the SiO_2 content (55.32–80.21%) of our samples was substantially higher than that of Fe-Si oxyhydroxides produced by the alteration of hydrothermal sulfides (Hekinian et al., 1993; Iizasa et al., 1998). In addition, sulfur content was measured to be low (0.18–0.39%). These results suggested that Fe-Si oxyhydroxides in our samples cannot be derived from the alteration of sulfides (Hekinian et al., 1993). However, observed slight enrichment in

https://doi.org/10.5194/bg-2019-315
Preprint. Discussion started: 4 September 2019
© Author(s) 2019. CC BY 4.0 License.

Biogeosciences Discussions

LREE with a pronounced positive Eu anomaly indicated that these deposits were likely to have formed by direct precipitation from hydrothermal fluids (Michard et al., 1983). In addition, elevated REE and P content was observed in the purple-red 34II-T22 deposit, which indicated that biogenic Fe-stalks may have played a significant role in the precipitation of the deposits. Therefore, we propose that microbes may have contributed to hydrothermal Fe-Si oxyhydroxide formation at the ultra-slow spreading SWIR.

5.2 Implications of Sr-Nd-Pb isotope content

The Sr-Nd-Pb isotopes of low-temperature hydrothermal Fe-Si deposits at the SWIR show a different sources. In order to map the peculiar isotope signature of our studied samples, the data have been plotted in Nd/Sr, Sr/Pb and Pb/Pb diagrams. Sr-Nd-Pb isotopes showed higher $^{87}Sr/^{86}Sr$, $^{207}Pb/^{204}Pb$, $^{208}Pb/^{204}Pb$ and lower $^{143}Nd/^{144}Nd$ and $^{206}Pb/^{204}Pb$ ratios compared to those of Mid Pacific Ridge (MPR) and Southeast Indian Ridge (SEIR) basalts (Fig. 7). This result may be closely associated with the ultra-slow spreading rate and the presence of robust magmatism at the SWIR (Dupré and Allègre, 1983; Allègre et al. 1984; Meyzen et al., 2005; Yang et al., 2017). The Sr isotope characteristics of the studied deposits are consistent with direct precipitation of Fe-Si oxyhydroxides from low-temperature hydrothermal fluids (Dekov et al., 2010; Yang et al., 2015). This indicates the deposits probably precipitated mainly from hydrothermal fluids mixed with a subsidiary amount of ambient seawater (Allègre et al., 1984; Severmann et al., 2004). Furthermore, the Sr-Nd isotopic plots of the Fe-Si deposits are very similar to the isotopic compositions

https://doi.org/10.5194/bg-2019-315
Preprint. Discussion started: 4 September 2019
© Author(s) 2019. CC BY 4.0 License.


observed in the Lilliput and Jan Mayen hydrothermal deposits (Devok et al., 2010; Johannessen et al., 2016). This probably indicates that the Nd isotope composition of the Fe-Si deposits was inherited from local parent basalts and seawater. The 34II-T22 and 20V-T8 deposits have particularly pronounced positive εNd values compared with the other samples (Table 2), which indicates that Nd content reflects the influence of hydrothermal fluids leaching from substrate rocks. The presence of a positive Eu anomaly in the Fe-Si deposits further supports this interpretation. We propose that the Sr and Nd isotope compositions of the Fe-Si deposits at the SWIR might be closely related to interaction of hydrothermal fluids and seawater.

The distinct Pb isotope compositions in the Fe-Si deposits compared to other geological settings (Fig. 7) clearly reflects the different isotopic compositions of Pb sources. The Pb isotope compositions of the studied samples were consistent with those of basalts from the same part of the SWIR (Yang et al., 2017). This confirms the role of basalt as a source of Pb in the low-temperature hydrothermal deposits. These conclusions are supported by the fact that that there was little variation in the Pb isotope composition of the Fe-Si deposits was observed, due to homogenization by hydrothermal circulation. Hamelin and Allègre (1985) discussed that Pb isotopic homogenization can be interpreted in terms of the SWIR being contaminated by a mantle source. Although melt supply is limited at the ultra-slow spreading SWIR, plume-ridge interaction may generate significant geochemical anomalies beneath the SWIR (Breton et al., 2013; Yang et al., 2017). Plume influence at the SWIR is supported by the presence of thicker crust and hotter mantle between the Indomed and

https://doi.org/10.5194/bg-2019-315
Preprint. Discussion started: 4 September 2019
© Author(s) 2019. CC BY 4.0 License.


Gallieni Fracture Zone (Sauter et al., 2009). We infer that the peculiar Pb isotope composition of Fe-Si deposits might be genetically linked to plume-ridge interactions at the SWIR.

5.3 Formation of biogenic Fe-oxyhydroxides at the SWIR

Microbial activity is a potential starting point for investigating the mechanisms that have contributed to the formation of hydrothermal Fe-Si deposits (Emerson et al. 2007; Edwards et al. 2011; Johannessen et al., 2016). Previous studies have shown that Fe(II) oxidation by Fe-oxidizing bacteria results in distinct morphologies of Fe-oxyhydroxides in hydrothermal deposits, microbial mats, and redox-stratified water columns (Edwards et al., 2011; Peng et al., 2015; Chan et al., 2016; Chiu et al. 2017). SEM analysis of the Fe-oxyhydroxides in this study indicated that microbes were widely involved in their precipitation at the SWIR (Fig. 4), with biogenic Fe-oxyhydroxides in the studied deposits exhibiting various morphologies and sizes. We observed two different types of rich-Fe biomineralized forms occurring in the deposits. In particular, abundant sheaths, stalks and filaments enriched in iron resemble those produced by *Gallionella ferruginea*, *L. ochracea*, and *M. ferrooxydans* (Edwards et al. 2011; Peng et al., 2015; Chan et al., 2016). Likewise, nanoSIMS ion mapping of discrete Fe-rich filaments provided further direct evidence for their formation by Fe oxidizing bacteria (Fig. 8). Furthermore, encrustation of spherical and rod-like forms clearly indicated that were of biogenic origin (Sun et al., 2015). The microbes encrusted by Fe-oxyhydroxides may be responsible for biologically induced mineralization (Ta et al., 2017). We suggest that two types of biomineralized

https://doi.org/10.5194/bg-2019-315
Preprint. Discussion started: 4 September 2019
© Author(s) 2019. CC BY 4.0 License.

Biogeosciences Discussions

505 deposits with distinct forms are produced either directly or indirectly at the SWIR
506 (Fortin and Langley, 2005; Mikutta et al., 2008; Peng et al., 2015; Chui et al., 2017).
507 In fact, the reduced iron contributed by hydrothermal systems fuels microbial
508 activity though the oxidation Fe(II) to Fe(III), which leads to the precipitation of
509 Fe-bearing minerals (Field et al., 2016; Makita et al., 2016). Some species of microbe
510 would be viable and active in situ, considering the relative abundance of ferric iron
511 oxides (oxyhydroxides) Fe_{OX1} and Fe_{OX2}, as revealed by iron speciation data (Fig. 6
512 and Table 4) (Chan et al., 2016; Johannessen et al., 2016). We observed that microbial
513 Mn(II) oxidization was responsible for the formation of the black layer in sample
514 DIV95-2, which had a low Fe_{OX1} content. However, as biogenic Fe-oxyhydroxides
515 were more abundant in samples DIV95-1, 34II-T22, 21V-T7 and 20V-T8, the Fe_{OX1}
516 content also increased. The Mössbauer results further suggested that octahedral Fe(III)
517 in our samples was the dominant Fe species, which was in good agreement with the
518 XRD results and iron speciation data (Figs. 5 and S2). No Fe(II) doublets were
519 detected in any of the samples based on Mössbauer data, indicating the hydrothermal
520 deposits formed in oxidizing microenvironments. Chan et al. (2016) showed that stalk
521 and sheath morphologies of Fe mats may reflect the redox conditions, and the
522 morphologies observed in this study indicate low concentrations of O_2 during
523 formation. Somewhat surprisingly, large amounts of reactive iron minerals such as
524 2-line-ferrihydrite and lepidocrocite can be identified in all deposits (Figs. 5 and 6).
525 As a result, bacterial oxidation of dissolved Fe(II) is expected to have produced the
526 2-line-ferrihydrite and lepidocrocite (Kappler and Newman, 2004; Larese-Casanova

https://doi.org/10.5194/bg-2019-315
Preprint. Discussion started: 4 September 2019
© Author(s) 2019. CC BY 4.0 License.

et al., 2010; Chan et al., 2011; Peng et al., 2015). Therefore, as mentioned above, these findings imply that biomineralization can effectively promote the precipitation of iron bearing minerals in modern and ancient hydrothermal fields.

5.4 Formation of biogenic silica

Well-preserved morphologies of biomineralized silica were common in all the Fe-Si deposits at the SWIR (Fig. 6), representing a link between oceanic crust and life (Zierenberg et al., 2000; Conley et al., 2017). The dissolved silica is thought to be primarily derived from hydrothermal fluids, based on the expected composition of hydrothermal fluids. Silica is not an essential nutrient for microbes found at hydrothermal sites (Baross and Hoffman, 1985; Martin et al., 2008). Based on mineral phase relationships and temperatures of precipitation deduced from stable isotopes of O, we infer that the precipitation of silica is probably driven by microbial activity. Morphologically similar sheaths, stalks, filaments, spheroidal and rod-like forms within the deposits may be regarded as biosignatures that can survive in low-temperature environments. The abundant structurally coordinated silica may allow the preservation of microbial primary features. This interpretation is in accordance with those of encased microbes observed in banded iron formations and ancient jaspers (Chi Fru et al., 2013; Grenne and Slack, 2003). Of particular note is the presence of abundant poorly reactive sheet silicate iron (Fe_{PRS}) in our samples (Table 4). It is likely that biogenic Fe-Si oxyhydroxides have been transformed into ordered poorly reactive sheet silicates, such as nontronite (Ueshima and Tazaki, 2001; Dekov et al., 2007; Sun et al., 2011). Previous studies have put forward two

https://doi.org/10.5194/bg-2019-315
Preprint. Discussion started: 4 September 2019
© Author(s) 2019. CC BY 4.0 License.


549 hypotheses for the precipitation of biogenic silica. Firstly, microbes may serve as
550 reactive geochemical surfaces where Si is directly adsorbed and precipitated (Juniper
551 and Fouquet, 1988; Ueshima and Tazaki, 2001; Jones et al., 2004; Peng and Jones,
552 2012). We observed many silicified spherical and rod-like microbes preserved in the
553 DIV-95-1 and 21V-T1 deposits (Figs. 6a and 6d). Biomineralization experiments
554 performed using a variety of marine microorganisms have demonstrated that
555 unsheathed bacteria can become encrusted in silica (Orange et al., 2009; Li et al.,
556 2013). The second hypothesis suggests interactions between Fe oxyhydroxide and
557 silica occur as a result of microbial activity (Dupraz and Visscher, 2005; Peng et al.,
558 2011; Sun et al., 2015). For instance, we found preformed silica colloids, which
559 measured few tens of nanometers in diameter, attached to the surface of Fe oxidizing
560 sheaths. Upon aging, the structurally coordinated Fe(III) becomes partially replaced
561 by amorphous Si, and is transformed into ordered Fe-Si oxyhydroxides (Fein et al.,
562 2002; Pokrovski et al., 2003; Devok et al., 2010). This interpretation is in accordance
563 with the existence of filamentous microfossils found in submarine hydrothermal vent
564 precipitates more than 3,770 million years ago (Dodd et al., 2017). We propose that
565 the geochemical constituents of mineralized microbes imply that dissolved silica and
566 ferric iron were original reactants in the low-temperature hydrothermal systems of the
567 SWIR. Given the morphological, mineralogical and geochemical characteristics of the
568 deposits, the ultra-slow spreading SWIR might be regarded as a potential region for
569 the origin and evolution of life.

https://doi.org/10.5194/bg-2019-315
Preprint. Discussion started: 4 September 2019
© Author(s) 2019. CC BY 4.0 License.

6 Conclusions

Fe-Si deposits collected from the ultra-slow spreading SWIR showed evidence of low-temperature hydrothermal origin. The deposits were mainly composed of 2-line ferrihydrite, pyrite, natrojarosite and amorphous opal, characterized by both negative Ce and positive Eu anomalies, along with a slight enrichment in LREE. The Sr-Nd-Pb isotopic compositions of the Fe-Si deposits were partially inherited from a mantle source mixed with seawater by low-temperature hydrothermal circulation. Two different types of biomineralized forms were preserved in Fe-Si deposits. These biogenic Fe-Si oxyhydroxides clearly showed that microbial activity played a significant role in the formation of the hydrothermal deposits, either directly or indirectly, due to biologically-induced mineralization. Mössbauer spectra and iron speciation data provided further insight into the iron-bearing phases in these deposits. These findings supported the hypothesis that microbial activity was the principal deposition mechanism of Fe-Si oxyhydroxides in modern and ancient seafloor hydrothermal systems. Such studies shed light on the possibility that the origin and evolution of life in an environment similar to the ultra-slow spreading SWIR.

Data availability. The data of the different experiments are freely available upon request from the corresponding author. Data sets supporting the results are also archived in an open-access database: https://doi.org/10.6084/m9.figshare.9521117.v1.

Author contributions. This work was conceived and supervised by ZW and XP, ZL

https://doi.org/10.5194/bg-2019-315
Preprint. Discussion started: 4 September 2019
© Author(s) 2019. CC BY 4.0 License.

592 and KT performed the measurements and data evaluation. KT wrote the paper with
593 contributions from all coauthors.
594
595 *Competing interests*. The authors declare that they have no conflict of interest.
596
597 *Acknowledgments*. Special thanks go to all of the participants of the cruise of the R/V
598 DaYang YiHao and XYH09 conducted by the China Ocean Mineral Resource R&D
599 Association (COMRA). This work is directly supported by the National Nature
600 Science Foundation of China (Grant No. 2016YFA0601100) and the National Natural
601 Science Foundation of China (Grant No.41176065). NanoSIMS analyses were
602 performed at the Institute of Geology and Geophysics, Chinese Academy of Sciences.
603 The Sr, Nd, and Pb isotopic compositions were performed in the Laboratory for
604 Radiogenic Isotope Geochemistry at the University of Science and Technology of
605 China.
606
607 **References**

608 Alt, J. C.: Hydrothermal oxide and nontronite deposits on seamounts in the Eastern Pacific, Mar.
609 Geol., 81, 227–239, https://doi.org/10.1016/ 0025-3227(88)90029-1, 1988.
610 Baross, J. A., and Hoffman, S. E.: Submarine hydrothermal vents and associated gradient
611 environments as sites for the origin and evolution of life, Origins. Life. Evol. B., 15, 327-345,
612 https://doi.org/10.1007/BF01808177, 1985.
613 Benjamin, S.B., and Haymon, R. M.: Hydrothermal mineral deposits and fossil biota from a young
614 (0.1 Ma) abyssal hill on the flank of the fast spreading East Pacifific Rise: evidence for
615 pulsed hydrothermal flow and tectonic tapping of axial heat and fluids, Geochem. Geoph.
616 Geosy., 7, Q05002, https://doi.org/10.1029/2005GC001011, 2006.

https://doi.org/10.5194/bg-2019-315
Preprint. Discussion started: 4 September 2019
© Author(s) 2019. CC BY 4.0 License.

617 Bernis, K., Lowell, R. P., and Farough, A.: Diffuse flow on and around hydrothermal vents at
618 mid-ocean ridges, Oceanography., 25, 182-191, https://doi.org/10.5670/oceanog.2012.16,
619 2012.
620 Berquó, T. S., Banerjee, S. K., Ford, R. G., Penn, R. L., and Pichler, T.: High crystallinity
621 Si-ferrihydrite: An insight into its Ne´el temperature and size dependence of magnetic
622 properties, J. Geophys. Res., 112, B02102, https://doi.org/10.1029/2006JB004583, 2007.
623 Boström, K., and Peterson, M. N. A.: The origin of aluminum-poor ferromanganoan sediments in
624 areas of high heat flow on the East Pacifific Rise, Mar. Geol., 7, 427–447, 1969.
625 Boyd, T. D., and Scott, S. D.: Microbial and hydrothermal aspects of ferric oxyhydroxides and
626 ferrosic hydroxides: The example of Franklin Seamount, Western Woodlark Basin, Papua
627 New Guinea, Geochem. T., 2, 45. https://doi.org/10.1186/1467-4866-2-45, 2001.
628 Breton, T., Nauret, F., Pichat, S., Moine, B., Moreira, M., Rose-Koga, E. F., Auclair, D., Bosq, C.,
629 and Wavrant, L.-M.: Geochemical heterogeneities within the Crozet hotspot, Earth. Planet. Sc.
630 Lett., 376, 126–136, https://doi.org/10.1016/j.epsl.2013.06.020, 2013.
631 Burkhard, D. J. M.: Iron-bearing silicate glasses at ambient conditions, J. Non-Cryst. Solids., 275,
632 175-188, https://doi.org/10.1016/S0022-3093(00)00252-0, 2000.
633 Cannat, M., Rommevaux-Jestin, C., Sauter, D., Deplus, C., and Mendel, V.: Formation of the axial
634 relief at the very slow spreading Southwest Indian Ridge (49° to 69°E), J. Geophys. Res., 104,
635 825–843, https://doi.org/10.1029/1999JB900195, 1999.
636 Chan, C. S., Fakra, S. C., Emerson, D., Fleming, E. J., and Edwards, K. J.: Lithotrophic
637 iron-oxidising bacteria produce organic stalks to control mineral growth: implications for
638 biosignature formation, ISME. J., 5, 717-727, https://doi.org/10.1038/ismej.2010.173, 2011.
639 Chan, C. S., McAllister, S. M., Leavitt, A. H., Glazer, B. T., Krepski, S. T., and Emerson, D.:
640 The architecture of iron microbial mats reflects the adaption of chemolithotrophic iron
641 oxidation in freshwater and marine environments, Front. Microbiol., 7:796,
642 https://doi.org/10.3389/fmicb.2016.00796, 2016.
643 Chaumba, J. B.: Hydrothermal Alteration in the Main Sulfide Zone at Unki Mine, Shurugwi
644 Subchamber of the Great Dyke, Zimbabwe: Evidence from Petrography and Silicates Mineral
645 Chemistry, Minerals. Basel., 7, 127, https://doi.org/10.3390/min7070127, 2017.
646 Chen, P., Zhang, L., Guo, X., Dai, X., Liu, L., Xi, L., Wang, J., Song, L., Wang, Y., Zhu, Y.,

https://doi.org/10.5194/bg-2019-315
Preprint. Discussion started: 4 September 2019
© Author(s) 2019. CC BY 4.0 License.

647 Huang, L., and Huang, Y.: Diversity, Biogeography, and Biodegradation Potential of
648 Actinobacteria in the Deep-Sea Sediments along the Southwest Indian Ridge, Front.
649 Microbiol., 7:1340, https://doi.org/10.3389/fmicb.2016.01340, 2016.
650 Chen, F., Hegner, E., and Todt, W.: Zircon ages and Nd isotopic and chemical compositions of
651 orthogneisses from the Black Forest, Germany: evidence for a Cambrian magmatic arc, Int. J.
652 Earth. Sci., 88, 791–802, https://doi.org/10.1007/s005310050306, 2000.
653 Chen, F., Li, X., Wang, X., Li, Q., and Siebel, W.: Zircon age and Nd-Hf isotopic composition of
654 the Yunnan Tethyan belt, southwestern China, Int. J. Earth. Sci., 96, 1179–1194,
655 https://doi.org/10.1007/s00531-006-0146-y, 2007
656 Chi Fru, E. et al.: Fossilized iron bacteria reveal a pathway to the biological origin of banded iron
657 formation, Nat. Commun., 4:2050, https://doi.org/10.1038/ncomms3050, 2013.
658 Chiu, B. K., Kato, S., McAllister, S. M., Field, E. K., and Chan, C. S.: Novel Pelagic
659 Iron-Oxidizing Zetaproteobacteria from the Chesapeake Bay Oxic–Anoxic Transition Zone,
660 Front. Microbiol., 8, 1280, https://doi.org/10.3389/fmicb.2017.01280, 2017.
661 Cole, D. R., Horita, J., Polyakov, V. B., Valley, J. W., Spicuzza, M. J., and Coffey, D. W.: An
662 experimental and theoretical determination of oxygen isotope fractionation in the system
663 magnetite-H_2O from 300 to 800 °C, Geochim. Cosmochim. Ac., 68, 3569-3585,
664 https://doi.org/10.1016/j.gca.2004.02.017, 2004.
665 Conley, D. J., Frings, P. J., Fontorbe, G., Clymans, W., Stadmark, J., Hendry, K. R., Marron, A.
666 O., and De La Rocha, C. L.: Biosilicifification Drives a Decline of Dissolved Si in the
667 Oceans through Geologic Time, Front. Mar. Sci., 4, 397,
668 https://doi.org/10.3389/fmars.2017.00397, 2017. .
669 Craddock, P. R., Bach, W., Seewald, J.S., Rouxel, O.J., Reeve,s E., andTivey, M. K.: Rare earth
670 element abundances in hydrothermal fluids from the Manus Basin, Papua New Guinea:
671 Indicators of sub-seafloor hydrothermal processes in back-arc basins, Geochim. Cosmochim.
672 Ac., 74, 5494-5513, https://doi.org/10.1016/j.gca.2010.07.003, 2010.
673 Dekov, V. M., Kamenov, G. D., Stummeyer, J., Thiry, M., Savelli, C., Shanks, W. C., Fortin, D.,
674 Kuzmann, E., and Vértes, A.: Hydrothermal nontronite formation at Eolo Seamount
675 (Aeolianvolcanic arc, Tyrrhenian Sea), Chem. Geol., 245, 103–119.
676 https://doi.org/10.1016/j.chemgeo.2007.08.006, 2007.

https://doi.org/10.5194/bg-2019-315
Preprint. Discussion started: 4 September 2019
© Author(s) 2019. CC BY 4.0 License.

677 Dekov, V. M., Petersen, S., Garbe-Schöberg, C. D., Kamenov, G. D., Perner, M., Kuzmann, E.,
678 and Schmidt, M.: Fe-Si-oxyhydroxide deposits at a slow spreading centre with thickened
679 oceanic crust: The Lilliput hydrothermal field (9°330 S, Mid-Atlantic Ridge), Chem. Geol.,
680 278, 186-200, https://doi.org/10.1016/j.chemgeo.2010.09.012, 2010.
681 Dick H. J. B., Lin J., and Schouten H.: An ultraslow-spreading class of ocean ridge, Nature., 426,
682 405–412, https://doi.org/10.1038/nature02128, 2003.
683 Dodd, M. S., Papineau, D., Grenne, T., et al.: Evidence for early life in Earth's oldest
684 hydrothermal vent precipitates, Nature., 543, 60-64, https://doi.org/10.1038/nature21377,
685 2017.
686 Dupraz, C., and Visscher P. T. Microbial lithification in marine stromatolites and hypersaline mats,
687 Trends. Microbiol., 13, 429–438, https://doi.org/10.1016/j.tim.2005.07.008, 2005.
688 Dupré, B., and Allègre, C. J.: Pb-Sr isotope variation in Indian Ocean basalts and mixing
689 phenomena, Nature., 303, 142–143, https://doi.org/10.1038/303142a0, 1983.
690 Edmonds, H. N., and German, C. R.: Particle geochemistry in the rainbow hydrothermal plume,
691 Mid-Atlantic Ridge, Geochim. Cosmochim. Ac., 68, 759-772,
692 https://doi.org/10.1016/S0016-7037(03)00498-8, 2004.
693 Edwards, K. J., Glazer, B. T., Rouxel, O. J., Bach, W., Emerson, D., Davis, R. E., Toner, B. M.,
694 Chan, C. S., Tebo, B. M., Staudigel, H., and Moyer, C. L. Ultra-diffuse hydrothermal venting
695 supports Fe-oxidizing bacteria and massive umber deposition at 5000 m of Hawaii, ISME. J.,
696 5, 1748–1758, https://doi.org/10.1038/ismej.2011.48, 2011.
697 Emerson, D., and Moyer, C. L.: Microbiology of Seamounts: Common Pattern observed in
698 Community Structure, Oceanography., 23, 148-163, https://doi.org/10.5670/oceanog.2010.67,
699 2010.
700 Emerson, D., and Moyer, C. L.: Neutrophilic Fe-oxidizing bacteria are abundant at the Loihi
701 Seamount hydrothermal vents and play a major role in Fe oxide deposition, Appl. Environ.
702 Microbiol., 68, 3085–3093, https://doi.org/10.1128/AEM.68.6.3085-3093.2002, 2002.
703 Emerson, D., Rentz, J. A., Lilburn, T. G., Davis, R. E., Aldrich, H., Chan, C., et al.: A novel
704 lineage of proteobacteria involved in formation of marine Fe-oxidizing microbial mat
705 communities, PLoS ONE., 2:e667, https://doi.org/10.1371/journal.pone.0000667, 2007.

https://doi.org/10.5194/bg-2019-315
Preprint. Discussion started: 4 September 2019
© Author(s) 2019. CC BY 4.0 License.

706 Fein, J. B., Scott, S., and Rivera, N.: The effect of Fe on Si adsorption by Bacillus subtilis cell
707 walls: insights into non-metabolic bacterial precipitation of silicate minerals, Chem.
708 Geol., 182, 265-273, https://doi.org/10.1016/S0009-2541(01)00294-7, 2002.
709 Field, E. K., Kato, S., Findlay, A. J., MacDonald, D. J., Chiu, B. K., Luther, G. W., et al.:
710 Planktonic marine iron oxidizers drive iron mineralization under low-oxygen conditions,
711 Geobiol., 14, 499–508, https://doi.org/10.1111/gbi.12189, 2016.
712 Fleming, E. J., Davis, R. E., McAllister, S. M., Chan, C. S., Moyer, C. L., Tebo, B. M., and
713 Emerson, D. Hidden in plain sight: Discovery of sheath-forming, iron-oxidizing
714 Zetaproteobacteria at Loihi Seamount, Hawaii, USA, FEMS. Microbiol. Ecol., 85, 116–27,
715 https://doi.org/10.1111/1574-6941.12104, 2013.
716 Fortin, D., and Langley, S.: Formation and occurrence of biogenic iron-rich minerals, Earth-Sci.
717 Rev., 72, 1-19, https://doi.org/10.1016/j.earscirev.2005.03.002, 2005.
718 Fortin, D., Ferris, F. G., and Scott, S. D.: Formation of Fe-silicates and Fe-oxides on bacterial
719 surfaces in hydrothermal deposits collected near the Southern Explorer Ridge in the
720 Northeast Pacifific Ocean, Am. Mineral., 83, 1399–1408,
721 https://doi.org/10.2138/am-1998-1102, 1998.
722 Gamo, T., et al.: Chemical characteristics of newly discovered black smoker fluids and associated
723 hydrothermal plumes at the Rodriguez Triple Junction, Central Indian Ridge, Earth. Planet.
724 Sc. Lett., 193, 371–379, https://doi.org/10.1016/S0012-821X(01)00511-8, 2001.
725 Georgen, J. E., Lin, J., and Dick, H. J. B.: Evidence from gravity anomalies for interactions of the
726 Marion and Bouvet hotspots with the Southwest Indian Ridge: Effects of transform offsets,
727 Earth. Planet. Sc. Lett., 187, 283–300, https://doi.org/10.1016/s0012-821x(01)00293-x, 2001.
728 German, C. R., Colley, S., Palmer, M. R., et al.: Hydrothermal plumeparticle fluxes at 13°N on the
729 East Pacific Rise, Deep-Sea Res. Pt. I., 49, 1921–1940,
730 https://doi.org/10.1016/S0967-0637(02)00086-9, 2002.
731 German, C. R., Bowen, A., Coleman, M. L., Honig, D. L., Huber, J. A., Jakuba, M. V., Kinsey, J.
732 C., Kurz, M. D., Leroy, S., McDermott, J. M. et al.: Diverse styles of submarine venting on
733 the ultraslow spreading Mid-Cayman Rise, P. Natl. Acad. Sci. USA., 107, 14020-14025,
734 https://doi:10.1073/pnas.1009205107, 2010.

https://doi.org/10.5194/bg-2019-315
Preprint. Discussion started: 4 September 2019
© Author(s) 2019. CC BY 4.0 License.

735 German, C. R., and Parson, L. M.: Distributions of hydrothermal activity along the mid-Atlantic
736 ridge: Interplay of magmatic and tectonic control, Earth. Planet. Sc. Lett., 160, 327–341,
737 https://doi.org/10.1016/S0012-821X(98)00093-4, 1998.
738 German, C. R., Klinkhammer, G. P., Edmond, J. E., Mitra, A., and Elderfield, H.: Hydrothermal
739 scavenging of rare-earth elements in the ocean, Nature., 345, 516-518,
740 https://doi.org/10.1038/345516a0(1990), 1990.
741 German, R., Baker, E. T., Mevel, C., Tamaki, K., and the FUJI Science Team.: Hydrothermal
742 activity along the southwest Indian ridge, Nature., 395, 490–493,
743 https://doi.org/10.1038/26730, 1998.
744 Gnaser, H.: Ionization probability of sputtered cluster anions: Cn^- and Sn^-, Appl. Surf. Sci., 203,
745 78–81, https://doi.org/10.1016/S0169-4332(02)00683-9, 2003.
746 Grenne, T. and Slack, J. F.: Bedded jaspers of the Ordovician Løkken ophiolite, Norway: seafloor
747 deposition and diagenetic maturation of hydrothermal plume-derived silica-iron gels, Miner.
748 Deposita., 38, 625–639, https://doi.org/10.1007/s00126-003-0346-3, 2003.
749 Hamelin, B. and Allègre, C. J.: Large-scale regional units in the depleted upper mantle revealed by
750 an isotope study of the South-West Indian Ridge, Nature., 315, 196–199,
751 https://doi.org/10.1038/315196a0, 1985.
752 Hein, J. R., Schulz, M. S., Dunham, R. E., Stern, R. J., and Bloomer, S. H.: Diffuse flow
753 hydrothermal manganese mineralization along the active Mariana and southern Izu-Bonin arc
754 system, western Pacific, J. Geophys. Res., 113, B08S14,
755 https://doi.org/10.1029/2007JB005432, 2008.
756 Hekinian, R., Hoffert, M., Larqué P., Cheminée, J. L., Stoffers, P., and Bideau, D.: Hydrothermal
757 Fe and Si oxyhydroxide deposits from South Pacifific intraplate volcanoes and East Pacifific
758 Rise axial and off-axial regions, Econ. Geol., 88, 2099–2121,
759 https://doi.org/10.2113/gsecongeo.88.8.2099, 1993.
760 Herrmann, A. M., Clode, P. L., Fletcher, I. R., Nunan, N., Stockdale, E. A., O'Donnel, A. G., and
761 Murphy, D. V.: A novel method for the study of the bphysical interface in soils using
762 nano-scale secondary ion mass spectrometry, Rapid. Commun. Mass. Sp., 21, 29–34,
763 https://doi.org/10.1002/rcm.2811, 2007.

https://doi.org/10.5194/bg-2019-315
Preprint. Discussion started: 4 September 2019
© Author(s) 2019. CC BY 4.0 License.

764 Hrischeva, E., and Scott, S. D.: Geochemistry and morphology of metalliferous sediments and
765 oxyhydroxides from the Endeavour segment, Juan de Fuca Ridge, Geochim. Cosmochim. Ac.,
766 71, 3476–3497, https://doi.org/10.1016/j.gca.2007.03.024, 2007.
767 Husson, L., Yamato, P., and Bézos, A.: Ultraslow, slow, or fast spreading ridges: Arm wrestling
768 between mantle convection and far-field tectonics, Earth. Planet. Sc. Lett., 429, 205-215,
769 https://doi.org/10.1016/j.epsl.2015.07.052, 2015.
770 Iizasa, K., Kawasaki, K., Maeda, K., Matsumoto, T., Saito, N., and Hirai, K.: Hydrothermal
771 sulfifide bearing Fe-Si oxyhydroxide deposits from the Coriolis Troughs, Vanuatu backarc,
772 southwestern Pacifific, Mar. Geol., 145, 1–21,
773 https://doi.org/10.1016/S0025-3227(97)00112-6, 1998.
774 Ji, F., Zhou, H., Yang, Q., Gao, H., Wang, H., and Lilley, M.: Geochemistry of hydrothermal vent
775 fluids and its implications for subsurface processes at the active longqi hydrothermal field,
776 southwest indian ridge, Deep-Sea Res. Pt. I., 122, 41-47,
777 https://doi.org/10.1016/j.dsr.2017.02.001, 2017.
778 Johannessen, K. C., Vander Roost, J., Dahle, H., Dundas, S. H., Pedersen, R. B., and Thorseth, I.
779 H.: Environmental controls on biomineralization and Fe-mound formation in a
780 low-temperature hydrothermal system at the Jan Mayen Vent fields, Geochim. Cosmochim.
781 Ac., 202, 101–123, https://doi.org/10.1016/j.gca.2016.12.016, 2016.
782 Johnston, J. H. and Lewis, D. G.: A detailed study of the transformation of ferrihydrite to hematite
783 in an aqueous medium at 92 °C, Geochim. Cosmochim. Ac., 47, 1823–1831,
784 https://doi.org/10.1016/0016-7037(83)90200-4, 1983.
785 Jones, B., Konhauser, K. O., Renaut, R. W., and Wheeler, R.: Microbial silicification in Iodine
786 Pool, Waimangu Geothermal area, North Island, New Zealand: implications for recognition
787 and identification of ancient silicified microbes, J. Geol. Soc., 162, 983-993,
788 https://doi.org/10.1144/0016-7649Er161-6A, 2004.
789 Juniper, S. K., and Fouquet, Y.: Filamentous iron–silica deposits from modern and ancient
790 hydrothermal sites, Can. Mineral., 26(1), 859–869, 1988.
791 Kappler, A., and Newman, D. K.: Formation of Fe(III)-minerals by Fe(II)-oxidizing
792 photoautotrophic bacteria, Geochim. Cosmochim. Ac., 68, 1217-1226,
793 https://doi.org/10.1016/j.gca.2003.09.006, 2004.

https://doi.org/10.5194/bg-2019-315
Preprint. Discussion started: 4 September 2019
© Author(s) 2019. CC BY 4.0 License.

794 Karl, D. M., Brittain, A. M. and Tilbrook, B. D.: Hydrothermal and microbial processes at
795 Loihi Seamount, a mid-plate hot-spot volcano, Deep-Sea Res. Pt. I., 36, 1655-1673,
796 https://doi.org/10.1016/0198-0149(89)90065-4, 1989.
797 Kita, I., Taguchi, S., and Matsubaya, O.: Oxygen isotope fractionation between amorphous silica
798 and water at 34–93 °C, Nature., 314, 83–84, https://doi.org/10.1038/314083a0, 1985.
799 Lagarec, K., and Rancourt, D. G.: Extended Voigt-based analytic lineshape method for
800 determining N-dimensional correlated hyperfifine parameter distributions in Mössbauer
801 spectroscopy, Nucl. Instrum. Meth. Phy. Res., 129, 266–280,
802 https://doi.org/10.1016/S0168-583X(97)00284-X, 1997.
803 Langley, S., Igric, P., Takahashi, Y., Sakai, Y., Fortin, D., Hannington, M. D., and Schwarz
804 Schampera, U.: Preliminary characterization and biological reduction of putative biogenic
805 iron oxides (BIOS) from the Tonga-Kermadec Arc, southwest Pacifific Ocean, Geobiol., 7,
806 35–49, https://doi.org/10.1111/j.1472-4669.2008.00180.x, 2009.
807 Larese-Casanova, P., Haderlein, S. B., and Kappler, A.: Biomineralization of lepidocrocite and
808 goethite by nitrate-reducing Fe(II)-oxidizing bacteria: effect of pH, bicarbonate, phosphate,
809 and humic acids, Geochim. Cosmochim. Ac., 74, 3721–3734,
810 https://doi.org/10.1016/j.gca.2010.03.037, 2010.
811 Li, J., K. Benzerara, Bernard S., and Beyssac, O.: The link between biomineralization and
812 fossilization of bacteria: insights from field and experimental studies, Chem.
813 Geol., 359, 49-69, https://doi.org/10.1016/j.chemgeo.2013.09.013, 2013.
814 Li, J., Jian H., Chen Y. J., Singh S. C., Ruan A., Qiu X., Zhao M., Wang X., Niu X., and Ni J.:
815 Seismic observation of an extremely magmatic accretion at the ultraslow spreading
816 Southwest Indian Ridge, Geophys. Res. Lett., 42, 2656–2663,
817 https://doi.org/10.1002/2014GL062521, 2015.
818 Lin, J. and Zhang, C.: The first collaborative China-international cruises to investigate mid-ocean
819 ridge hydrothermal vents, InterRidge News., 15, 33-34, 2006.
820 Makita, H., Tanaka, E., Mitsunobu, S., Miyazaki, M., Nunoura, T., Uematsu, K., et al.:
821 Mariprofundus micogutta sp. nov., a novel iron-oxidizing zetaproteobacterium isolated from
822 a deep-sea hydrothermal fifield at the Bayonnaise knoll of the Izu-Ogasawara arc, and a

https://doi.org/10.5194/bg-2019-315
Preprint. Discussion started: 4 September 2019
© Author(s) 2019. CC BY 4.0 License.

description of Mariprofundales ord. nov. and Zetaproteobacteria classis nov, Arch. Microbiol., 199, 335–346, https://doi.org/10.1007/s00203-016-1307-4, 2016.

Martin, W., Baross, J., Kelley, D., and Russell, M. J.: Hydrothermal vents and the origin of life, Nat. Rev. Microbiol., 6, 805-814, https://doi.org/10.1038/nrmicro1991, 2008.

Meyzen, C. M., Ludden, J. N., Humler, E., Luais, B., Toplis, M. J., Me´vel, C., and Storey, M.: New insights into the origin and distribution of the DUPAL isotope anomaly in the Indian Ocean mantle from MORB of the Southwest Indian Ridge, Geochem. Geophys. Geosyst., 6:Q11K11, https://doi.org/10.1029/2005GC000979, 2005.

Michard, A., Albaréde, F., Michard, G., Minster, J.F., and Charlou, J. L.: CharlouRare-earth elements and uranium in high temperature solutions from East Pacific Rise hydrothermal vent field, Nature., 303,795-797, https://doi.org/10.1038/303795a0, 1983.

Michard, G., Albarede, F., Michard, A., Minster, J.F., Charlou, J. L., and Tan N.: Chemistry of solutions from the 13°N East Pacific Rise hydrothermal site, Earth. Planet. Sc. Lett., 67, 297-307, https://doi.org/10.1016/0012-821X(84)90169-9, 1984.

Mikutta, C., Mikutta, R., Bonneville, S., Wagne,r F., Voegelin, A., Christl, I., and Kretzschmar, R.: Synthetic coprecipitates of exopolysaccharides and ferrihydrite. Part I: characterization, Geochim. Cosmochim. Ac., 72, 1111-1127, https://doi.org/10.1016/j.gca.2007.11.035, 2008.

Mills, R. A., Alt J. C., and Clayton T.: Low-temperature flfluid flflow through sulfifidic sediments from TAG: Modifification of flfluid chemistry and alteration of mineral deposits, J. Geophys. Res., 23, 3495–3498, https://doi.org/10.1029/96GL02885, 1996.

Mitra, A., Elderfield, H., and Greaves, M.: Rare earth elements in submarine hydrothermal fluids and plumes from the Mid-Atlantic Ridge, Mar. Chem., 46, 217-235, https://doi.org/10.1016/0304-4203(94)90079-5, 1994.

Murad, E., and Cashion, J.: Mössbauer Spectroscopy of Environmental Materials and Industrial Utilization, Kluwer Academic Publisher, Boston, pp. 159–223, https://doi.org/10.1007/978-1-4419-9040-2, 2004.

Murad, E., and Johnston, J. H.: Mössbauer Spectroscopy Applied to Inorganic Chemistry ed G J Long (New York: Plenum). Publisher, Springer, Boston, MA, pp 507–92, https://doi.org/10.1007/978-1-4899-0462-1, 1987.

https://doi.org/10.5194/bg-2019-315
Preprint. Discussion started: 4 September 2019
© Author(s) 2019. CC BY 4.0 License.

852 Murad, E., and Schwertmann, U.: The Mössbauer spectrum of ferrihydrite and its relations to
853 those of other iron oxides, Am. Mineral., 65, 1044–1049, https://doi.org/000.3-00'4X/80/09 r
854 0-l 044$02.0, 1980.
855 Murad, E.: The Mossbauer spectrum of “well” crystallized ferrihydrite, J. Magn. Magn. Mater., 74,
856 153–157, https://doi.org/10.1016/0304-8853(88)90062-5, 1988.
857 Niu, X., Ruan A., Li, J., Minshull, T. A., Sauter, D., Wu, Z. , Qiu, X., Zhao, M., Chen, Y. J., and
858 Singh, S.: Along-axis variation in crustal thickness at the ultraslow spreading Southwest
859 Indian Ridge (50°E) from a wide-angle seismic experiment, Geochem. Geophys. Geosyst.,
860 16, 468–485, https://doi.org/10.1002/2014GC005645, 2015.
861 Oh, S. J., Cook D. C., and Townsend H. E.: Characterization of iron oxides commonly formed as
862 corrosion products on steel, Hyperfine. Interact., 112, 59–65,
863 https://doi.org/10.1023/A:1011076308501, 1998.
864 Orange, F., Westall, F., Disnar, J. R., Prieur, D., Bienvenu, N., Leromancer, M., and Defarge, C.:
865 Experimental silicification of the extremophilic Archaea Pyrococcus abyssi and
866 Methanocaldococcus jannaschii: applications in the search for evidence of life in early Earth
867 and extraterrestrial rocks, Geobiol., 7, 403–418,
868 https://doi.org/10.1111/j.1472-4669.2009.00212.x, 2009.
869 Peng X., and Jones B.: Rapid precipitation of silica (opal-A) disguises evidence of biogenicity in
870 high-temperature geothermal deposits: Case study from Dagunguo hot spring, China,
871 Sediment. Geol., 257-260, 45-62, https://doi.org/10.1016/j.sedgeo.2012.01.013, 2012.
872 Peng, X., Chen, S., Zhou, H., Zhang, L., Wu, Z., Li, J., Li, J., and Xu, H.: Diversity of biogenic
873 minerals in low-temperature Si-rich deposits from a newly discovered hydrothermal field on
874 the ultraslow spreading Southwest Indian Ridge, J. Geophys. Res.-Biogeo., 116, G03030,
875 https://doi.org/10.1029/2011JG001691, 2011.
876 Peng, X., Chen S., and Xu H.: Formation of biogenic sheath-like Fe oxyhydroxides in a
877 near-neutral pH hot spring: Implications for the origin of microfossils in high-temperature,
878 Fe-rich environments, J. Geophys. Res.-Biogeo., 118, 1397–1413,
879 https://doi.org/10.1002/jgrg.20119, 2013.

https://doi.org/10.5194/bg-2019-315
Preprint. Discussion started: 4 September 2019
© Author(s) 2019. CC BY 4.0 License.

880 Peng, X., Ta K., Chen S., Zhang L., and Xu H.: Coexistence of Fe(II)- and Mn(II)-oxidizing
881 bacteria govern the formation of deep sea umber deposits, Geochim. Cosmochim. Ac., 169,
882 200–216, https://doi.org/10.1016/j.gca.2015.09.011, 2015.
883 Pokrovski, G. S., Schott, J., Farges, F., and Hazemann, J. L.: Iron (III)-silica interactions in
884 aqueous solution: insights from X-ray absorption fine structure spectroscopy, Geochim.
885 Cosmochim. Ac., 67, 3559-3573, https://doi.org/10.1016/S0016-7037(03)00160-1, 2003.
886 Poulton, S., and Canfifield, D.: Development of a sequential extraction procedure for iron:
887 implications for iron partitioning in continentally derived particulates, Chem. Geol., 214,
888 209–221, https://doi.org/10.1016/j.chemgeo.2004.09.003, 2005.
889 Sauter, D., Cannat, M., Meyzen, C., Bezos, A., Patriat, P., Humler, E., and Debayle, E.:
890 Propagation of a melting anomaly along the ultraslow Southwest Indian Ridge between 46°E
891 and 52°200 E: Interaction with the Crozet hotspot? Geophys. J. Int., 179, 687–699,
892 https://doi.org/10.1111/j.1365-246X.2009.04308.x, 2009.
893 Severmann, S., Mills R. A., Palmer M. R., and Fallick A. E.: The origin of clay minerals in active
894 and relict hydrothermal deposits, Geochim. Cosmochim. Ac., 68, 73–88,
895 https://doi.org/10.1016/S0016-7037(03)00235-7, 2004.
896 Singer, E., Emerson, D., Webb, E. A., Barco, R. A., Kuenen, J. G., Nelson, W. C., Chan, C. S.,
897 Comolli, L. R., Ferriera, S., Johnson, J., Heidelberg, J. F. , and Edwards, K. K.:
898 Mariprofundus ferrooxydans PV-1 the First Genome of a Marine Fe(II) Oxidizing
899 Zetaproteobacterium. PLoS ONE., 6, e25386, https://doi.org/10.1371/journal.pone.0025386,
900 2011.
901 Sun, Z., Zhou H., Glasby G. P., Yang Q., Yin X., Li J., and Chen Z.: Formation of Fe-Mn-Si oxide
902 and nontronite deposits: Examples from hydrothermal fields on the Valu Fa Ridge, Lau Basin,
903 J. Asian. Earth. Sci., 43, 64–76, https://doi.org/10.1016/j.jseaes.2011.08.011, 2012.
904 Sun, Z., Li J., Huang W., Dong H., Little C. T. S., and Li. J.: Generation of hydrothermal Fe-Si
905 oxyhydroxide deposit on the Southwest Indian Ridge and its implication for the origin of
906 ancient banded iron formations, J. Geophys. Res.-Biogeo., 120, 187–203,
907 https://doi:10.1002/2014JG002764, 2015.
908 Ta, K., Peng X., Chen S., Xu H., Li J., Du M., Hao J., and Lin Y.: Hydrothermal nontronite
909 formation associated wth microbes from low-temperature diffuse hydrothermal vents at the

https://doi.org/10.5194/bg-2019-315
Preprint. Discussion started: 4 September 2019
© Author(s) 2019. CC BY 4.0 License.

South Mid-Atlantic Ridge, J. Geophys. Res.-Biogeo., 122, 2375-2392, https://doi.org/10.1002/2017JG003852, 2017.

Tao, C., Lin J.,Guo S., Chen Y. J., Wu G., Han X., German C. R., Yoerger D. R., Zhou N., and Li H.: First active hydrothermal vents on an ultraslow-spreading center: Southwest Indian Ridge, Geology., 40, 47–50, https://doi.org/10.1130/G32389.1, 2012.

Tivey, M. K.: Generation of seafloor hydrothermal vent fluids and associated mineral deposits, Oceanography., 20, 50–65, https://doi.org10.5670/oceanog.2007.80, 2007.

Toner, B. M., Santelli C. M., Marcus M. A., Wirth R., Chan C. S., McCollom T., Bach W., and Edwards K. J.: Biogenic iron oxyhydroxide formation at mid-ocean ridge hydrothermal vents: Juan de Fuca Ridg, Geochim. Cosmochim. Ac., 73, 388–403, https://doi.org/10.1016/j.gca.2008.09.035, 2009.

Ueshima, M., and Tazaki K.: Possible role of microbial polysaccharides in nontronite formation, Clay. Clay. Miner., 49, 292–299, https://doi.org/10.1346/CCMN.2001.0490403, 2001.

Vlastélic, I., Aslanian D., Laure Do., Henri B., Olivet, J. L. and Géli, L.: Large-scale chemical and thermal division of the Pacific mantle, Nature., 399, 345-350, https://doi.org/10.1038/20664, 1999.

Wade, M. L., Agresti, D. G., Wdowiak, T. J., Armendarez, L. P., and Farmer, J.: A Mössbauer investigation of iron-rich terrestrial hydrothermal vent systems: Lessons for Mars exploration, J. Geophys. Res.-Planet., 104(E4), 8489-8507, https://doi.org/0148-0227/99/1998 JE900049509.00, 1999.

Yang, A., Zhao T., Zhou M., and Deng X.: Isotopically enriched N-MORB: A new geochemical signature of off-axis plume-ridge interaction-A case study at 50°280 E, Southwest Indian Ridge, J. Geophys. Res.-Sol. Ea., 122, 191–213, https://doi.org/10.1002/2016JB013284, 2017.

Yang, B., Zeng, Z. and Wang, X.: Characteristics of Sr, Nd and Pb isotopic compositions of hydrothermal Si-Fe-Mn-oxyhydroxides at the PACMANUS hydrothermal field, Eastern Manus Basin, Acta. Oceanol. Sin., 34, 27-34, https://doi.org/10.1007/s13131-015-0706-8, 2015.

Yu, Z., Li, J., Niu, X., Rawlinson, N., Wang, W., Hu, H., Wei, X., Zhang, J., Lian, Y.: Lithospheric structure and tectonic processes constrained by microearthquake activity at the

https://doi.org/10.5194/bg-2019-315
Preprint. Discussion started: 4 September 2019
© Author(s) 2019. CC BY 4.0 License.

central ultraslow, J. Geophys. Res.-Sol. Ea., 123, 6247-6262, https://doi.org/10.1029/2017JB015367, 2018.

Zhang, B., Li, Z., Hou, Z., Zhang ,W., and Xu, B.: Mineralogy and Chemistry of Sulfides from the Longqi and Duanqiao Hydrothermal Fields in the Southwest Indian Ridge, Acta. Geol. Sin., 92, 1798-1822, https://doi.org/10.1111/1755-6724.13678, 2018.

Zhang, T., Lin J., and Gao J.: Magmatism and tectonic processes in Area A hydrothermal vent on the Southwest Indian Ridge, Sci. China. Earth. Sci., 56, 2186–2197, https://doi.org/10.1007/s11430-013-4630-5, 2013.

Zhao, M., et al.: Three-dimensional seismic structure of the Dragon Flag oceanic core complex at the ultraslow spreading Southwest Indian Ridge (49°390 E), Geochem. Geophys. Geosyst., 14, 4544–4563, https://doi.org/10.1002/ggge.20264, 2013.

Zhou, Y., Zhang, D., Zhang ,R., Liu, Z., Tao, C., Lu, B., Sun, D., Xu, P., Lin, R., Wang, J., and Wang, C.: Characterization of vent fauna at three hydrothermal vent fields on the Southwest Indian Ridge: Implications for biogeography and interannual dynamics on ultraslow-spreading ridges, Deep-Sea Res. Pt. I., 123, 1-12, https://doi.org/10.1016/j.dsr.2018.05.001, 2018.

Zhou, H., and Dick, H. J. B.: Thin crust as evidence for depleted mantle supporting the Marion Rise, Nature., 494, 195–200, https://doi.org/10.1038/nature11842, 2013.

Zierenberg, R. A., Adams, M. W. W., and Arp, A. J.: Life in extreme environments: Hydrothermal vents, P. Natl. Acad. Sci. USA., 97, 12961-12962, https://doi.org/10.1073/pnas.210395997, 2000.

https://doi.org/10.5194/bg-2019-315
Preprint. Discussion started: 4 September 2019
© Author(s) 2019. CC BY 4.0 License.

964 **Figure captions**

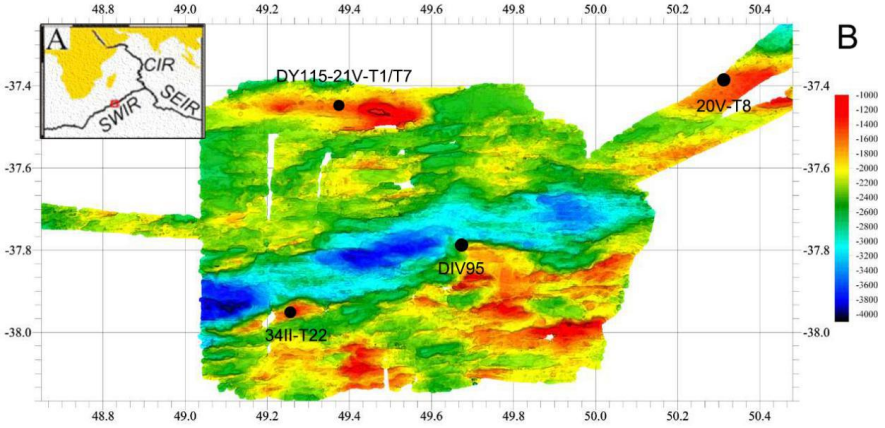

965 Figure 1. Regional bathymetric map and location of the sampling site at the SWIR.
966 Black dots represent sample locations in this study.

967

968

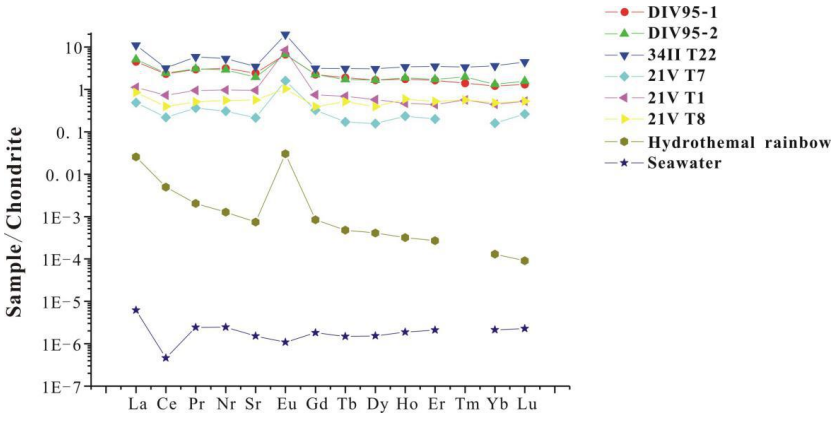

969 Figure 2. Chondrite-normalized REE distribution patterns of the hydrothermal Fe-Si
970 deposits in this study.

https://doi.org/10.5194/bg-2019-315
Preprint. Discussion started: 4 September 2019
© Author(s) 2019. CC BY 4.0 License.

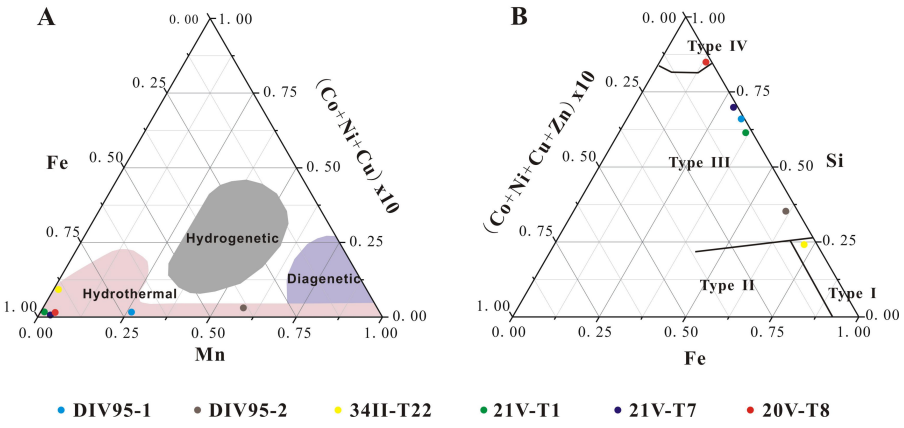

971 Figure 3. (a) Ternary diagram for Mn-Fe-(Co + Ni + Cu) ×10 of Fe-Si deposits. The
972 hydrothermal, diagenetic and hydrogenous fields were classified by Hein et al. (1994).
973 The Fe-Si deposits of this study are inferred to be of hydrothermal origin. (b)
974 Fe-Si-(Co + Ni + Cu + Zn) ×10 ternary diagram showing the various types of Fe-Si
975 deposits from Hekinian et al. (1993).

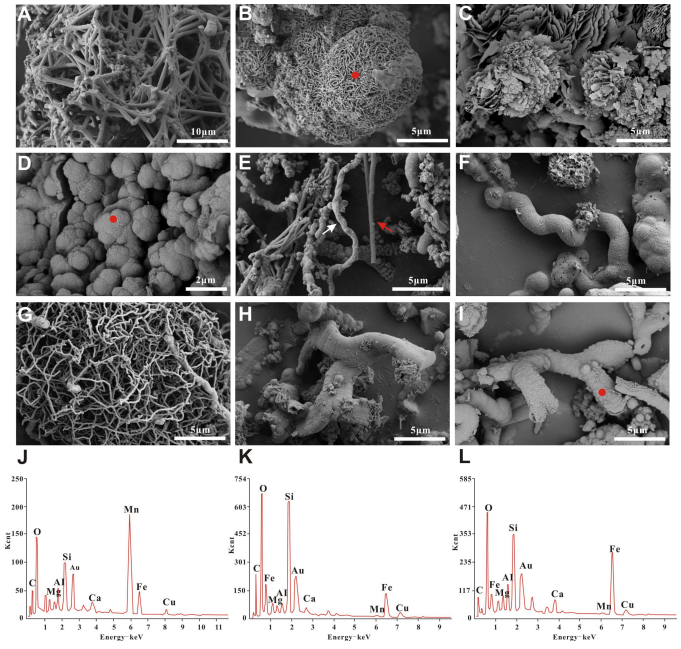

976 Figure 4. SEM images showing different styles of biogenic mineral structures in
977 different Fe-Si deposits. (a) A network-like structure composed of rod-like

https://doi.org/10.5194/bg-2019-315
Preprint. Discussion started: 4 September 2019
© Author(s) 2019. CC BY 4.0 License.

978 mineralized forms observed in the orange-yellowish sample DIV95-1. (b) Spheroidal
979 Mn-oxide surface showing honeycomb microtextures in the black sample DIV95-2. (c)
980 Typically rosette spherical structures observed in the DIV95-2 deposits. (d) Spherical
981 morphologies encrusted by iron and silicon in the yellowish sample 21V-T1. (e)
982 Ribbon-like helical filaments (white arrow) and hollow tubes (red arrow) found in the
983 purple-red sample 34II-T22. (f) Twisted stalk observed in the 34II-T22 deposit. (g) A
984 network-like structure composed of threadlet filaments observed in the brown sample
985 21V-T7. (h) Branched sheaths observed in the brown sample 20V-T8. (i) Spheroids
986 scattered on the surface of a branched sheath found in the brown sample 20V-T8. (j)
987 EDS from the area defined by the red dot in panel b. (k) EDS from the area defined by
988 the red dot in panel d. (l) EDS from the area defined by the red dot in panel i.

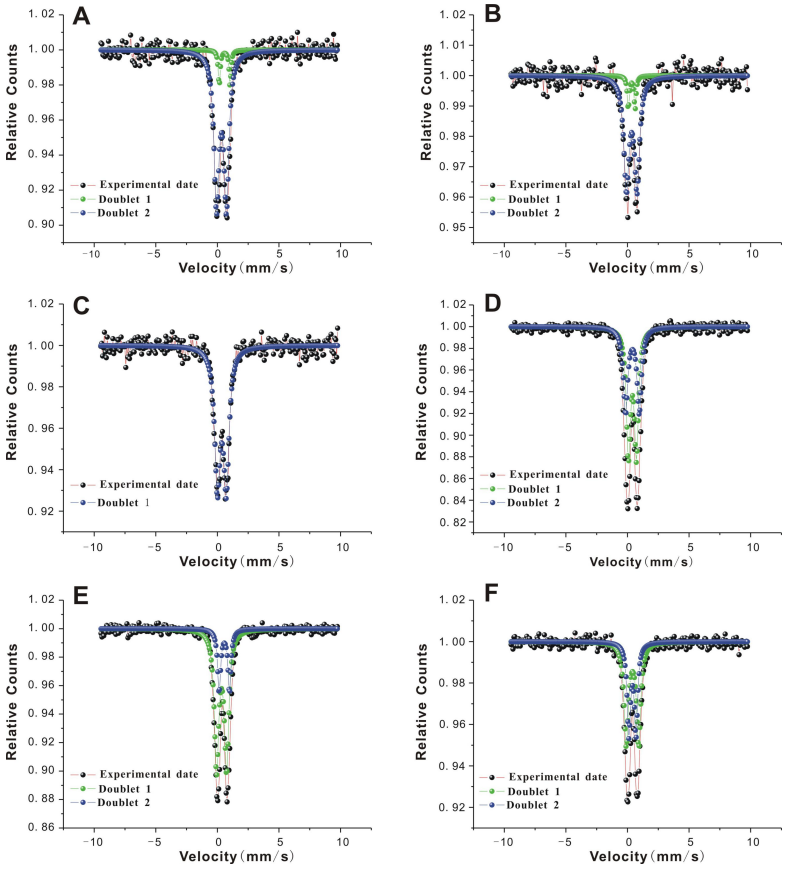

989 Figure 5. ^{57}Fe Mössbauer spectra at room temperature (300 K), and fitting results of

https://doi.org/10.5194/bg-2019-315
Preprint. Discussion started: 4 September 2019
© Author(s) 2019. CC BY 4.0 License.

990 Fe-Si deposits from the SWIR. (a) DIV95-1, (b) DIV95-2, (c) 34II-T22, (d) 21V-T1,
991 (e) 21V-T7, (f) 20V-T8.

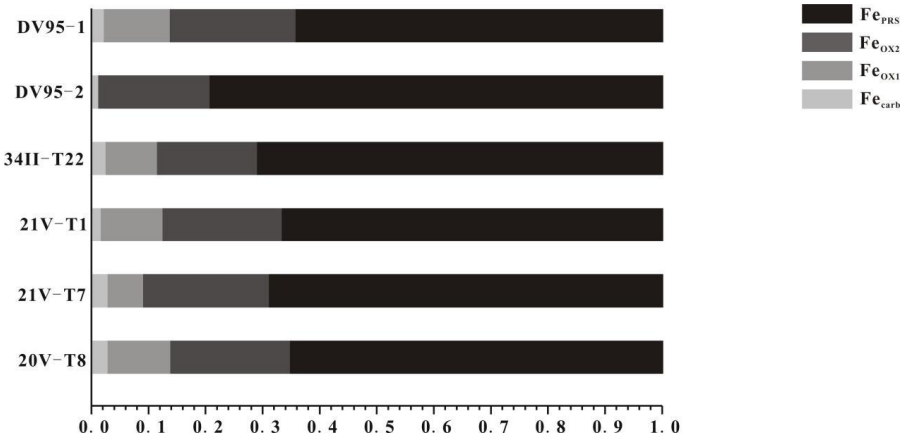

992 Figure 6. Sequential extraction of iron minerals in the studied Fe-Si deposits.

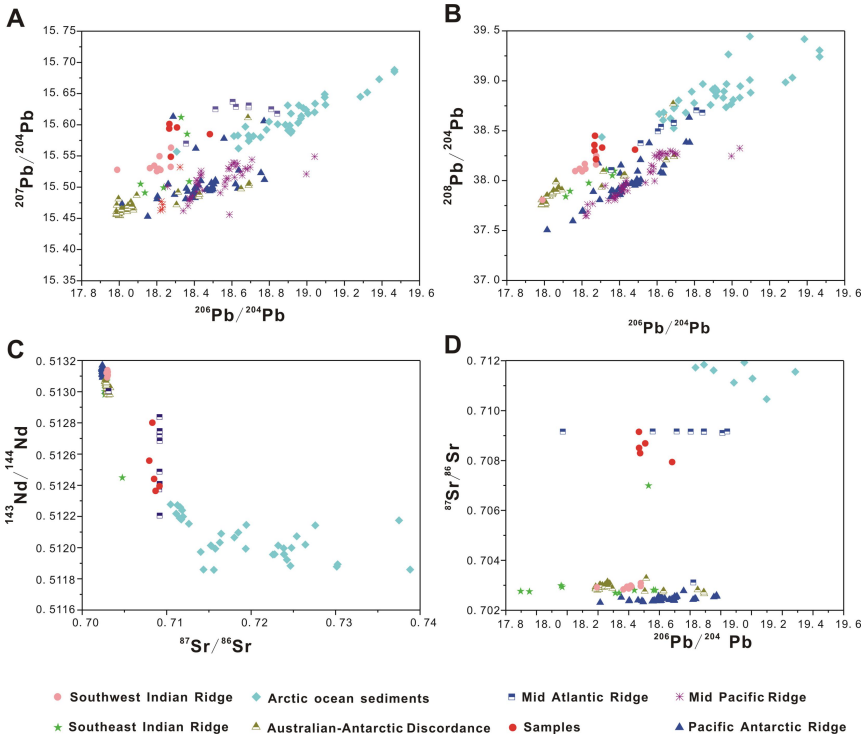

993 Figure 7. Comparison of $^{208}Pb/^{204}Pb$ versus $^{206}Pb/^{204}Pb$ (a), $^{207}Pb/^{204}Pb$ versus
994 $^{206}Pb/^{204}Pb$ (b), $^{87}Sr/^{86}Sr$ versus $^{143}Nd/^{144}Nd$ (c), and $^{87}Sr/^{86}Sr$ versus $^{206}Pb/^{204}Pb$ from

https://doi.org/10.5194/bg-2019-315
Preprint. Discussion started: 4 September 2019
© Author(s) 2019. CC BY 4.0 License.

995 the studied Fe-Si deposits, compared against Pacific Ridge basalts (Vlastèlic et al.,
996 1999), Arctic Ocean sediments (Maccali et al., 2018), Southeast Indian Ridge basalts
997 (Hamelin and Allègre, 1985), Australian-Antarctic Discordance basalts (Kempton et
998 al., 2002), Pacific hydrothermal sulfides (Fouquet and Marcoux, 1995), Atlantic
999 Ridge hydrothermal deposits (Dekov et al., 2010), and Southwest Indian Ridge basalts
1000 (Yang et al., 2017).
1001

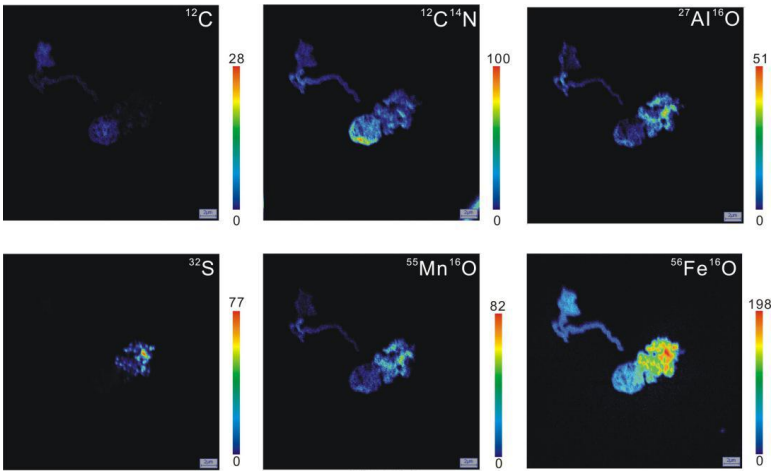

1002 Figure 8. NanoSIMS ionic images of $^{12}C^-$, $^{12}C^{14}N^-$, $^{32}S^-$, $^{27}Al^{16}O^-$, $^{55}Mn^{16}O^-$, and
1003 $^{56}Fe^{16}O_2^-$ from a twisted stalk. Ion intensity variations are shown by calibration bars.
1004 The scale bar is 2 μm for each panel.

https://doi.org/10.5194/bg-2019-315
Preprint. Discussion started: 4 September 2019
© Author(s) 2019. CC BY 4.0 License.

Table 1. Chemical composition (XRF and ICP-MS) of hydrothermal Fe-Si deposits at the SWIR.

Sample#	Al_2O_3 (wt.%)	CaO	Fe_2O_3	K_2O	MgO	MnO	Na_2O	P_2O_5	TiO_2	SiO_2	CuO	SO_3	Cr_2O_3	Co_2O_3	ZnO	Al/(Al+Fe+Mn)	Fe/Mn	TOTAL
DIV95-1	0.089	1.013	23.257	0.501	0.641	7.356	4.620	0.453	0.005	55.316	0.083	0.377	0.069	0.049	0.025	0.002	2.78	95.63
DIV95-2	0.096	1.704	32.964	0.581	0.851	25.467	4.777	0.264	0.007	27.220	0.159	0.180	0.063	0.073	-	0.001	1.41	99.20
34II-T22	0.031	0.696	64.733	0.06	1.396	0.124	2.101	0.898	0.004	27.076	0.294	0.295	0.006	0.018	0.177	0.001	460.17	97.90
21V-T7	0.053	0.382	21.695	0.278	0.591	0.741	3.865	0.149	0.004	68.356	-	0.396	-	0.024	0.05	0.002	25.81	98.85
21V-T1	0.072	0.506	23.216	0.294	0.664	0.516	3.364	0.356	0.004	68.106	-	0.307	-	0.061	0.040	0.002	39.65	97.73
20V-T8	0.059	0.387	10.562	0.182	0.237	0.124	1.892	0.335	0.004	85.205	-	0.184	-	0.026	0.0235	0.002	75.08	99.61

Sample#	Li (ppm)	Be	Sc	V	Cr	Co	Ni	Cu	Zn	Rb	Sr	Y	Zr	Nb	Mo	In	Cs	Ba	Tl
DIV95-1	55.325	0.230	0.669	87.225	4.104	13.210	27.647	313.016	155.360	7.618	230.843	3.994	2.067	0.110	115.621	0.030	0.399	254.107	2.636
DIV95-2	263.918	0.020	4.789	158.651	4.928	42.197	54.383	1095.661	253.322	8.297	343.394	4.159	4.079	0.240	420.370	0.070	0.370	682.089	4.259
34II-T22	1.747	0.220	0.988	675.981	16.069	232.846	23.085	1960.176	1478.588	1.757	296.921	10.290	10.939	0.409	168.771	0.240	0.269	46.889	2.575
21V-T7	1.454	0.538	2.609	71.919	3.355	0.767	2.589	10.514	79.814	2.858	221.541	0.438	1.195	0.090	82.373	0.010	0.279	943.514	0.149
21V-T1	6.082	0.739	0.210	39.647	1.618	1.059	4.154	40.396	126.830	1.348	253.959	1.128	2.127	4.983	42.773	0.010	0.040	926.755	0.499
20V-T8	18.321	0.080	0.360	39.871	1.010	1.279	3.848	69.487	44.309	1.769	141.332	1.129	1.059	0.740	22.189	0.000	0.020	420.797	0.750

Biogeosciences
Discussions
Open Access
EGU

https://doi.org/10.5194/bg-2019-315
Preprint. Discussion started: 4 September 2019
© Author(s) 2019. CC BY 4.0 License.

Biogeosciences
Discussions
Open Access
EGU

Sample#	Pb (ppm)	Bi	Th	U	Hf	Ta	La	Ce	Pr	Nd	Sm	Eu	Gd	Tb	Dy	Ho	Er	Tm	Yb
DIV95-1	2.257	0.070	0.030	12.601	0.040	0.170	1.657	2.227	0.409	2.237	0.559	0.579	0.689	0.110	0.629	0.150	0.409	0.050	0.300
DIV95-2	3.609	0.080	0.050	11.446	0.080	0.380	1.869	2.319	0.420	2.059	0.450	0.590	0.690	0.100	0.630	0.160	0.430	0.070	0.330
34II-T22	54.065	0.180	0.100	43.854	0.130	0.289	4.082	3.054	0.808	3.813	0.808	1.727	0.968	0.180	1.168	0.289	0.878	0.120	0.898
21V-T7	1.932	0.020	0.010	6.681	0.030	0.199	0.179	0.209	0.050	0.219	0.050	0.139	0.100	0.010	0.060	0.020	0.050	0.000	0.040
21V-T1	1.818	0.080	0.040	6.611	0.030	3.126	0.409	0.699	0.130	0.689	0.220	0.739	0.230	0.040	0.220	0.040	0.110	0.020	0.110
20V-T8	4.558	0.040	0.010	0.510	0.020	0.850	0.310	0.380	0.070	0.390	0.130	0.090	0.120	0.030	0.150	0.050	0.130	0.020	0.120

Sample#	Lu (ppm)	ΣREE	LREE	HREE	Eu/Eu*	Ce/Ce*	La_N/Yb_N	La_N/Sm_N	Fe/ΣREE
DIV95-1	0.050	10.054	7.668	2.386	2.850	0.644	3.74	1.86	1.57
DIV95-2	0.060	10.177	7.708	2.469	3.230	0.616	3.83	2.61	2.20
34II-T22	0.170	18.963	14.292	4.671	5.957	0.388	3.07	3.17	2.32
21V-T7	0.010	1.135	0.846	0.289	5.935	0.534	3.04	2.26	12.99
21V-T1	0.020	3.675	2.886	0.789	9.979	0.738	2.81	1.17	4.29
20V-T8	0.020	2.009	1.369	0.640	2.165	0.607	1.74	1.50	3.91

Ce/Ce*=$2Ce_N/(La_N+Pr_N)$; Eu/Eu*=$2Eu_N/(Sm_N+Gd_N)$

https://doi.org/10.5194/bg-2019-315
Preprint. Discussion started: 4 September 2019
© Author(s) 2019. CC BY 4.0 License.

1012 **Table 2.** Pb, Sr, Nd,and O isotopic data for studied samples and deduced temperature.

Sample#	$^{87}Sr/^{86}Sr$	(2σ)	$^{143}Nd/^{144}Nd$	(2σ)	$^{206}Pb/^{204}Pb$	(2σ)	$^{207}Pb/^{204}Pb$	(2σ)	$^{208}Pb/^{204}Pb$	(2σ)	$^{147}Sm/^{144}Nd$	εNd	$\delta^{18}O$ (‰ SMOW)	Deduced temperture (°C)
DIV95-1	0.708509	0.000014	0.512441	0.000011	18.2674	0.0029	15.6013	0.0036	38.2964	0.0119	0.1416	-3.8	20.908	43.23
DIV95-2	0.708686	0.000013	0.512364	0.000011	18.3076	0.0027	15.5957	0.0029	38.3313	0.0096	0.1298	-5.3	/	/
34II-T22	0.70915	0.000012	0.512801	0.000015	18.2664	0.002	15.5939	0.002	38.3574	0.0061	0.1180	3.2	35.87	114.66
21V-T1	0.708519	0.000015	0.512332	0.000015	18.2694	0.0016	15.6404	0.0036	38.4493	0.0062	0.1645	-6	17.352	31.17
21V-T7	0.707937	0.000013	0.512578	0.000031	18.4829	0.0026	15.5851	0.0028	38.3103	0.0092	0.1924	-1.2	16.564	28.76
20V-T8	0.708297	0.000012	0.512801	0.000015	18.2749	0.0009	15.5488	0.0011	38.2145	0.0034	0.1721	3.2	20.525	41.83

1013
1014
1015
1016

Biogeosciences
Discussions
Open Access
EGU

https://doi.org/10.5194/bg-2019-315
Preprint. Discussion started: 4 September 2019
© Author(s) 2019. CC BY 4.0 License.

1017 Table 3. Mössbauer parameters (room temperature) of hydrothermal Fe-Si deposits at
1018 the SWIR.

Sample#	IS	QS	LW	A (%)	Assignment	Mineralogy
DIV95-1	0.59	0.87	0.19	8.50	$^{VI}Fe^{3+}$	**Octahedral ferrihydrite**
	0.33	0.79	0.49	91.50	$^{VI}Fe^{3+}$	**2-line-ferrihydrite**
DIV95-2	0.34	0.55	0.19	10.40	$^{IV}Fe^{3+}$	**Lepidocrocite**
	0.34	0.85	0.50	89.60	$^{VI}Fe^{3+}$	**2-line-ferrihydrite**
34II-T22	0.36	0.72	0.53	100.00	$^{VI}Fe^{3+}$	**2-line-ferrihydrite**
21V-T1	0.40	0.65	0.40	57.40	$^{VI}Fe^{3+}$	**Goethite**
	0.40	1.11	0.44	42.60	$^{VI}Fe^{3+}$	**Octahedral ferrihydrite**
21V-T7	0.34	0.71	0.43	75.70	$^{VI}Fe^{3+}$	**2-line-ferrihydrite**
	0.56	0.84	0.3	24.30	$^{VI}Fe^{3+}$	**Octahedral Fe(III)**
20V-T8	0.40	1.01	0.42	58.70	$^{VI}Fe^{3+}$	**Octahedral ferrihydrite**
	0.40	0.58	0.33	41.30	$^{VI}Fe^{3+}$	**Lepidocrocite**

1019
1020 A=relative spectral area, IS=isomer shift, QS=quadrupole splitting, LW=line-width.
1021
1022
1023
1024
1025
1026
1027
1028
1029
1030
1031
1032
1033
1034
1035
1036
1037
1038
1039
1040
1041
1042

https://doi.org/10.5194/bg-2019-315
Preprint. Discussion started: 4 September 2019
© Author(s) 2019. CC BY 4.0 License.

Biogeosciences Discussions Open Access EGU

1043 Table 4. Relative compositions of Fe-bearing minerals of hydrothermal Fe-Si deposits
1044 at the SWIR.

Sample[#]	Fe_{carb} (μmol/g)	Fe_{ox1} (μmol/g)	Fe_{ox2} (μmol/g)	Fe_{PRS} (μmol/g)
DIV95-1	19.83	116.43	221.07	647.46
DIV95-2	11.38	0.40	223.21	910.60
34II-T22	28.70	111.71	218.13	885.64
21V-T1	15.60	117.16	225.90	723.42
21V-T7	27.11	63.95	226.51	710.03
20V-T8	28.27	118.48	224.89	703.17

1045
1046
1047
1048
1049
1050
1051
1052